NONINTRUSIVE SYSTEM FOR REPLICATION OF INTERLAYER PRINTED CIRCUIT PATTERNS

M. Chai and A. Chau

February 1998

Prepared for
U.S. Air Force AFMC, Hill AFB
Under Contract No. F42650-97-C-0038

19990421 021

DTIC QUALITY INSPECTED 4

REPORT DOCUMENTATION PAGE

Public reporting burden for this collection of information is estimated to average 1 hour per response, including the time for reviewing instructions, searching existing data sources, gathering and maintaining the data needed, and completing and reviewing the collection of information. Send comments regarding this burden estimate or any other aspect of this collection of information, including suggestions for reducing this burden, to Washington Headquarters Services, Directorate for information Operations and Reports, 1215 Jefferson Davis Highway, Suite 1204, Arlington, VA 22202-4302, and to the Office of Management and Budget, Paperwork Reduction Project (0704-0188), Washington, DC 20503.

1. AGENCY USE ONLY (*Leave blank*)	2. REPORT DATE February 1998	3. REPORT TYPE AND DATES COVERED Phase I Final Report, May 5, 1997-January 31, 1998

4. TITLE AND SUBTITLE

Nonintrusive System for Replication of Interlayer Printed Circuit Patterns

5. FUNDING NUMBERS

F42650-97-C-0038

6. AUTHOR(S)

M. Chai

7. PERFORMING ORGANIZATION NAME(S) AND ADDRESS(ES)

QUEST Integrated, Inc.
21414 68th Ave. S.
Kent, WA 98032

8. PERFORMING ORGANIZATION REPORT NUMBER

QUEST Technical Report
No. 779

9. SPONSORING/MONITORING AGENCY NAME(S) AND ADDRESS(ES)

OO-ALC/TIET
5851 F Ave., Bldg. 849
Hill AFB, UT 84056-5713

10. SPONSORING/MONITORING AGENCY REPORT NUMBER

11. SUPPLEMENTARY NOTES

12a. DISTRIBUTION/AVAILABILITY STATEMENT

Approved for public release; distribution unlimited.

12b. DISTRIBUTION CODE

13. ABSTRACT (*Maximum 200 words*)

Report developed under SBIR contract. The overall objective of this Phase I research program was to develop a nonintrusive method to image the art work of interlayer printed circuit board. Using forward Compton scattering and innovative design of a high-efficiency and high-resolution ring-slit Compton scattering camera, we have both theoretically demonstrated and experimentally verified the feasibility of reverse engineering the circuit board.. An algorithm using 2-D projection and Compton scattering data was proposed for image reconstruction of the layout of the printed circuit board, layer by layer. This algorithm is highly efficient, less computational, straightforward, and easy to implement.

14. SUBJECT TERMS "SBIR Report"

Nondestructive evaluation
Printed circuit board
Image processing
Forward Compton scattering
x-ray imaging

15. NUMBER OF PAGES
45

16. PRICE CODE

17. SECURITY CLASSIFICATION OF REPORT Unclassified	18. SECURITY CLASSIFICATION OF THIS PAGE Unclassified	19. SECURITY CLASSIFICATION OF ABSTRACT Unclassified	20. LIMITATION OF ABSTRACT Unlimited

i

TABLE OF CONTENTS

LIST OF FIGURES

1. INTRODUCTION

The purpose of this Phase I SBIR program conducted by QUEST Integrated, Inc., was to demonstrate the feasibility of developing a nonintrusive method and system for replication of the interlayer printed electronic circuit patterns from multi-layer printed circuit boards. Using forward Compton scattering and innovative detector design, we demonstrated that it is feasible to reverse engineer the circuit board. The new detector design allows us to gain three orders of magnitude more photon counts compared with conventional designs. We recommend that QUEST be considered to participate in the Phase II effort to design and construct a functional system.

This Phase I final report describes the results of the work including development of the following important innovations and findings:

1. Model-based feasibility evaluation. We used the Klein-Nishina model as the base model and calculated the optimal X-ray energy, and the signal intensity of, and signal contrast between copper trace and G10 circuit board substrate. We established theoretically the feasibility of using Compton scattering as a viable imaging tool for nonintrusive reconstruction of multi-layer printed circuit boards.

2. Innovative design of a high-efficiency and high-resolution ring-slit Compton scattering camera. Using a model-based system performance evaluation approach, the optimal design parameters for the camera were obtained and a system using these parameters was constructed.

3. Experimental verification of the feasibility using a scale experiment. The through-depth structure of copper trace in a scaled circuit board has been detected using the ring-slit camera.

4. Innovative image reconstruction algorithm. An algorithm using 2-D projection and Compton scattering data was proposed for image reconstruction of the layout of the printed circuit board layer by layer. This algorithm is highly efficient, less computational, straightforward and easy to implement.

This final report begins with a description of the Phase I technical objectives. This is followed by the project task breakdown, which describes the work carried out in this program. The next section presents the results obtained for each of these tasks. The final section provides a discussion of the project's technical merit and Phase II recommendations.

2. PHASE I TECHNICAL OBJECTIVES

The Phase I technical objectives included the following:

1. Develop a model to establish system parameters for the detailed system design.

2. Evaluate the performance of commercial systems and components for the final system design.

3. Based on the image data obtained from the evaluation of commercial systems, select image processing algorithms for generating the binary image data for input to circuit board fabrication tools.

4. Provide a detailed description of the proposed method and design the system to achieve the resolution and contrast ratio required for the replication of multi-layer printed circuit boards.

3. PHASE I WORK – TASK BREAKDOWN

3.1 Task 1. Theoretical Model

In this task, we examined the kinematics and quantum electrodynamics to determine the net efficiency of Compton scattering as a photon attenuation mechanism. The results of the section had served as the theoretical bases for system design, parameter optimization, and system evaluation.

3.2 Task 2. System Parameter Optimization

In this task, we determined the optimization conditions for system efficiency and system resolution for both a pinhole camera and a ring-slit camera based on a geometric model and the theory developed in Task 1. The efficiency of a ring-slit camera is more than three orders of magnitude higher than that of a pinhole camera. With a commercially available micro-focus X-ray tube such as FeinFocus, the photons received by the detector was estimated to be about $10^2 \sim 10^3$ per second for the ring-slit camera.

3.3 Task 3. System Design and Construction

In this task, a pinhole camera and a ring-slit camera were designed and constructed. The ring-slit camera is designed with the capability of imaging both 2-D projections in transmitted mode and through-depth structures in forward scattering mode.

3.4 Task 4. Experiment Results

Several experiments were carried out using both the pinhole camera and the ring slit camera. System resolution and efficiency and relative scattering intensities of several different circuit board substrate materials, including G10, were measured. Copper structures in a fabricated circuit were successfully detected.

3.5 Task 5. Image Reconstruction

In this task, a high-efficiency and low-computational algorithm that combines information from both the 2-D projection and Compton scattering was proposed for image reconstruction. A high-level software structure for image reconstruction and high-level hardware/software interaction were also designed.

4. PHASE I RESULTS

4.1 Task 1. Theoretical Model

4.1.1 Klein-Nishina Model

Compton scattering is the result of the incoherent interaction between the incident X-ray photons and the electrons of the sample host of interest. The cross section of this interaction (probability of the scattering process) is described by the Klein-Nishina quantum-electrodynamics model in the form:

$$\sigma(E_0,\theta) = \frac{r_0^2}{2}(\frac{E'}{E_0})^2(\frac{E'}{E_0}+\frac{E_0}{E'}-\sin^2 2\theta) \tag{1}$$

where r_0 is the classical electron radius, E_0 is the energy of the incident X-ray photon, E' is the energy of the scattered photons, and 2θ is the scattering angle.

Figure 1 is a polar plot of the angular dependence of the photon flux at two energy levels (30 KeV and 200 KeV). The scattering is forward biased. The higher the incident energy the more anisotropic the scattering is. At 500 KeV the forward scattering around 0 degree is 5 times that around 180 degrees. Below 10 KeV the scattering essentially becomes Thomson scattering (the elastic scattering).

4.1.2 Kinematics of Incoherent Scattering

The energy distribution of the scattered photon as a function of scattering angle is given by the following equation obtained through kinematic argument (independent of the quantum-electrodynamics):

$$E' = \frac{E_0}{1+\alpha(E_0)(1-\cos(2\theta)}, \tag{2}$$

where $\alpha(E_0)=\dfrac{E_0}{m_e c^2}$, and m_e, the rest mass of an electron. The quantity $m_e c^2$ is about 0.5 MeV.

Figure 2 shows the angular dependence of the ratio of the scattered photon to the incident photon at two energy levels (30 and 200 KeV). For incident photon energy less than 50 KeV, there is very little energy degradation. The photons at these energy levels are mostly coherent scattered (Rayleigh scattering). The energy degradation efficiency increases drastically at higher energy with marked forward biased anisotropy.
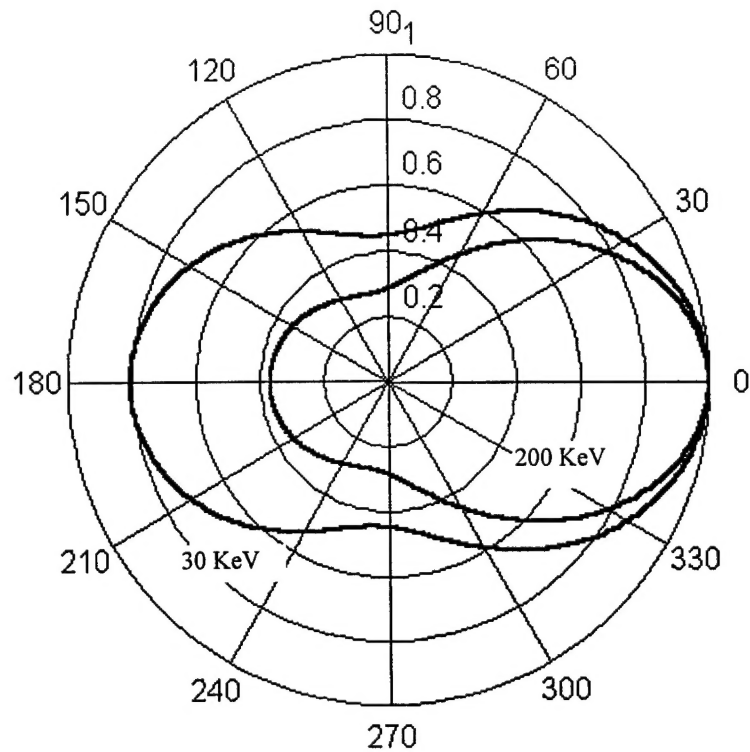
Figure 1. Angular Distribution of the Compton Scattering Cross Section
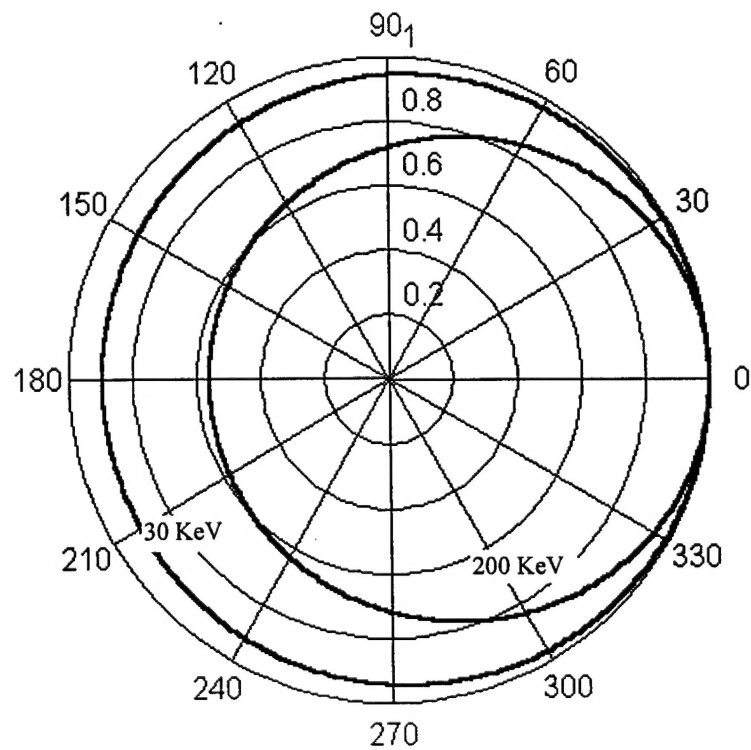
Figure 2. Angular Distribution of the Energy Ratio of the Scattered Photons Versus the Incident

4.1.3 Angular Dependence of the Scattered Photon Flux over the Energy 30~200 KeV Range

Equations (1) and (2) can be combined to eliminate E', and the angular dependence of the Compton scattering cross section over the entire energy range of incident photons can be calculated as

$$\sigma(\theta) = \int \frac{r_e^2}{2} \frac{1+\cos^2\theta + \dfrac{\alpha(E)^2(1-\cos\theta)^2}{1+\alpha(E)(1-\cos\theta)}}{(1+\alpha(E)(1-\cos\theta))^2} dE .$$ (3)

Equation (3) can be numerically evaluated. Figure 3 shows the angular dependence of this integration between 0-180 degrees over the energy range of 30 - 200 KeV. The cross section for small angles is much larger than that at large angles.

4.1.4 Total Flux Scattered by the Sample and Received by the Detector

The flux (or the intensity) of the Compton scattered X-ray off an element of the sample volume into a solid angle Ω defined by the detector can be estimated by the following equation:

$$\varphi_{out} = \varphi_{in} ZN\sigma(E_0) \frac{\Omega}{4\pi} te^{-\mu l} ,$$ (4)

where φ_{in} is the X-ray photon flux arriving at the element volume, Z is the atomic number of the sample, N is the number of electrons per unit volume (cm^{-3}), Ω is the solid angle defined by the detection, μ is the linear absorption coefficient of the element, t is the thickness of the element along the path of the X-ray, and l is the scattering path length inside the sample. This equation is of fundamental importance and will be used to determine the optimal design parameters. The quantity $ZN\sigma(E_0)$ up to 200 KeV is about 0.1 for Cu and about 0.03 for G10.

Figure 3. Angular Distribution of the Compton Scattered Photons over the Energy Range of 30 - 200 KeV

4.1.5 Most Efficient Energy Range for the Source

The kinematic and quantum electrodynamics effects are summarized as follows:

- The E'/E_0 ratio decreases with an increase of incident photon energy.
- The E'/E_0 ratio decreases with an increase of scattering angle.
- The higher the incident energy, the more forward biased the scattering.
- The larger the incident energy, the lower the total probability of Compton scattering.

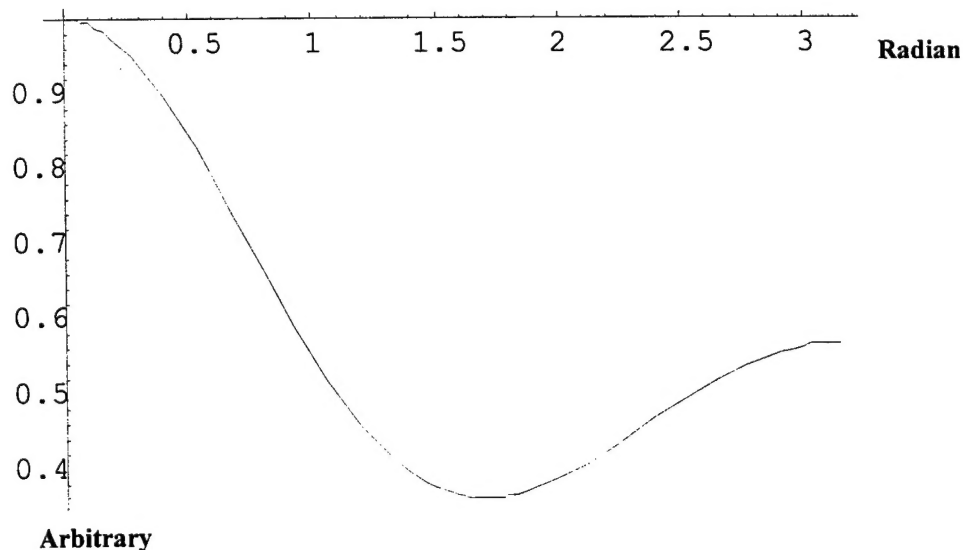As a result of these opposing factors, the ability of Compton scattering to degrade photon energy will increase monotonically to approximately 1 MeV, and will then fall off monotonically toward higher incident photon energies. Incoherent scattering will be an effective mechanism for degrading photon energy for incident photon energy in the range from circa 200 KeV to 5 MeV. Below and above these energy limits, it is not an effective mechanism for degrading photon energy.

4.1.6 The Calculated Attenuation for Cu and G10

The linear attenuation coefficient of the circuit board is of great importance, since it not only gives intensity attenuation along the path of the incident beam, but also the relative intensity of the scattered X-ray light between the trace and the substrate. This ratio will determine the contrast of the scattering image.

We assume that the artwork of the circuit board is made of copper and that the substrate can be represented by G10. The linear attenuation coefficient of the circuit board can be calculated as a function of energy. The expected signal contrast between copper and G10 substrate can be estimated.

The linear attenuation coefficient is defined as follows:

$$I = I_0 \exp(-\mu l), \tag{5}$$

where I_0 is the intensity of the incident X-ray, and I is the intensity after it travels through a path length l in the sample. The linear attenuation coefficient is a combination of several processes:

$$\mu = \mu(photoelectric) + \sigma(Compton) + k(pair). \tag{6}$$

Although these processes may coexist at certain energy ranges, each process dominates at a different energy level. For example, the attenuation due to pair production is only important at energy levels above 5 MeV, so it will not be considered for our application.

If the sample is a compound of n elements, then the linear attenuation coefficient can be written as:

$$\mu = (\frac{\mu_1}{\rho_1} + \frac{\mu_2}{\rho_2} + ... + \frac{\mu_n}{\rho_n})\rho_c, \tag{7}$$

where μ_i and ρ_i are the linear attenuation coefficient and density of i-th element, respectively, and ρ_c is the effective density of the compound.

G10 is a typical printed circuit board substrate material. It is a mixture of epoxies and fiberglass. The major components are H, Na, Ca, C, Si and Cl. The linear attenuation of both G10 and copper due to photoelectric process and Compton scattering are calculated and plotted in Figures 4 and 5.
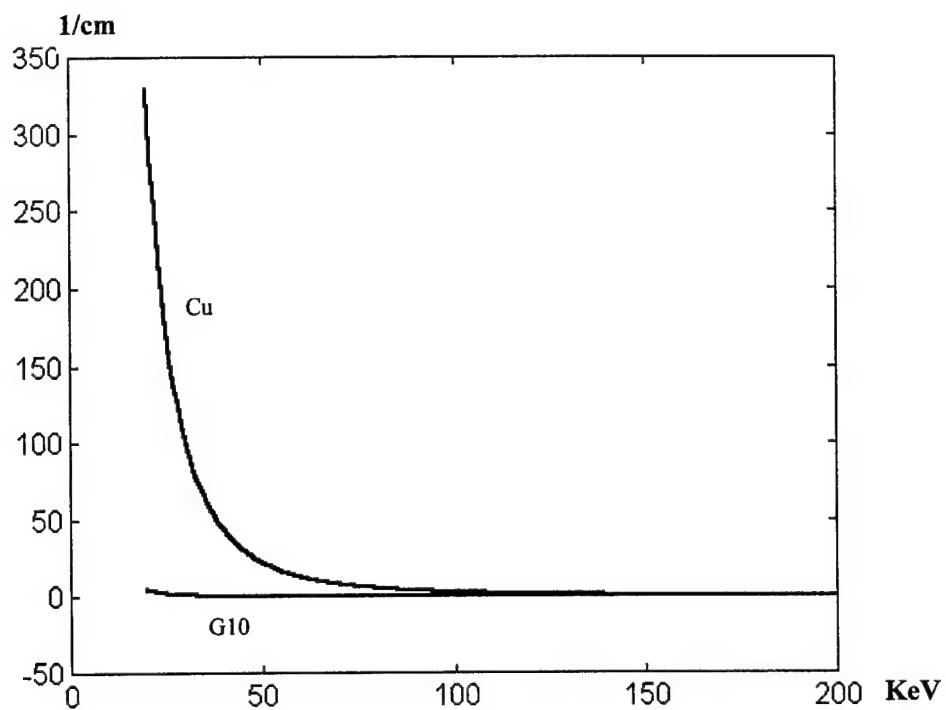
Figure 4. Linear Attenuation of Cu and G10 Due to Photoelectric Effect
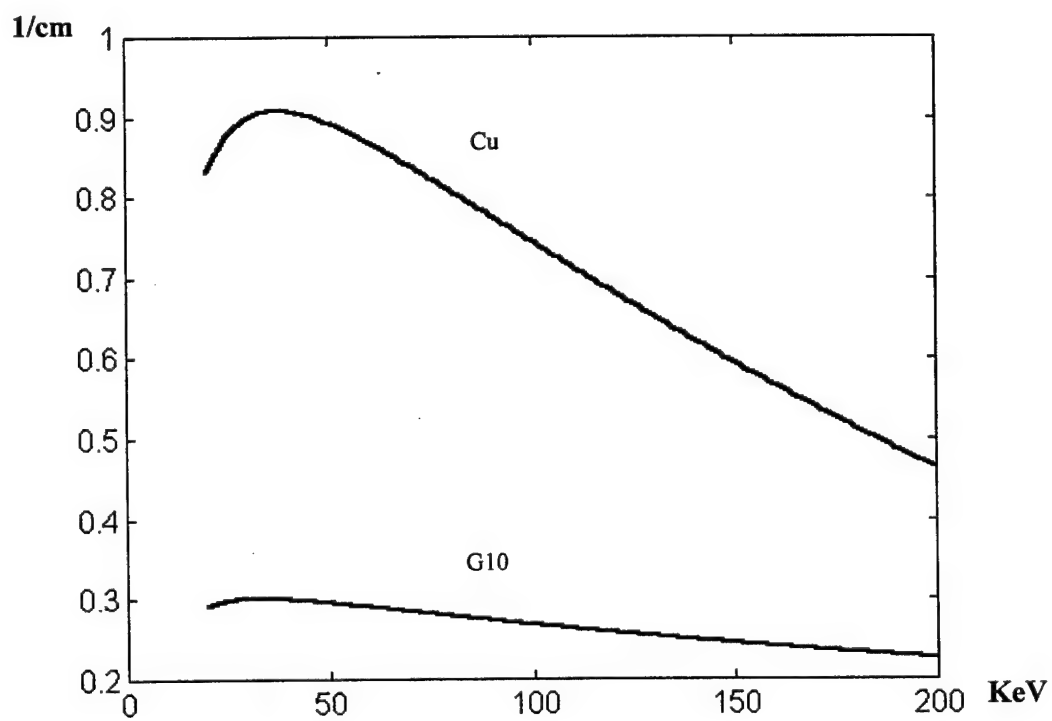

Figure 5. Linear Attenuation of Cu and G10 Due to Compton Scattering

From these figures, several conclusions can be drawn:

- Attenuation due to the photoelectric process decreases drastically with energy and is only important at energy levels below 50 KeV.

- Between 30 - 500 KeV, the dominant attenuation process is Compton scattering. The attenuation coefficient is relatively flat with energy.

- The contrast of scattered X-ray intensity between copper and G10 between 30 - 500 KeV is expected to vary between 3 and 2.

4.2 Task 2. Optimization of System Parameters

4.2.1 General Statement of the Problem

The key to the success of this is the flux of Compton scattered photon at the detector. Factors that affect the photon flux include the power, particularly the power density, and the physical dimensions of the X-ray sources, the physical properties of the sample, and the geometric arrangement of the detection system.

The photon flux intensity falls inversely to the square of the distance between the X-ray source and the sample (the circuit board) and, between the sample and the detector, it is required that both the X-ray source and the detector be placed as close to the sample as possible. This requirement is significantly limited by the sizes and consequently the interference of the X-ray source and the detector assembly if they are to be placed on the same side of the circuit boards. Since the circuit boards are unstuffed and accessible from both sides, we propose to use forward scattering, that is, to place the X-ray source and the detector on either side of the circuit boards. Under the same conditions otherwise, the photon flux in the forward configuration will be much higher than in the back scattering configuration.

The forward scattering configuration is also favored by the angular distribution of the Compton scattering. As discussed in the first section, at high energy levels, there are more forward scattering than back scattering. For example, at 500 KeV, approximately 5 times more photons are scattered through a unit solid angle around 0 degree than through a unit solid angle around 180 degrees.

Some assumptions are made for the design optimization based on both the information provided in the solicitation abstract and experimental conditions. These key assumptions are as follows:

- The traces are all about 25 micron (0.001 inch) thick.

- The densest spacing between the layers is 122 microns (0.005 inch).

- The substrate materials can be represented with G10.

- Scattering is important only along the primary path. The second and higher-order scattering are not considered.

- Within the circuit board, the X-ray is treated as a pencil beam.

First, we want to find the optimal conditions due solely to the geometry of the cameras (as opposed to the geometric dependence of the Compton scattering, which will be considered later). There are two opposing factors that concern the optimization of the design parameters for the detector assembly: the flux and the resolution. The resolution of the image of the circuit board through a pinhole on the detector plane (see Figure 6) is normally given, in form of convolution, by the following:

$$I_d = \frac{1}{M^2} I_t(\frac{x_d}{M}, \frac{y_d}{M}) ** h(x_d, y_d),$$ (8)

where, $h(x, y)$ is the point spread function (or impulse respond) of the pinhole; $I_t(x, y)$, the distribution of the scattering intensity of the circuit board; and $M = -\frac{L}{R}$, the magnification.

From Equation (4), the geometric constraints on the total flux depend on the magnitude of the photon flux of the incident beam and the size of the solid angle to the detector. Equations (4) and (8) could be used to optimize the photon flux for a given resolution. However, Equation (8) holds true only when the impulse respond is spatially invariant. In practice, the impulse respond varies significantly, particularly when the copper trace is far away from the optical axis of the camera. Instead, we are going to use a geometric argument to provide the constraints on the resolution of the image, which gives an exact solution to this problem. The part of Equation (4) related to the flux is

$$\varphi_{out} = \varphi_{in} \frac{\Omega}{4\pi} t.$$ (9)

The incident flux can be expressed as $\varphi_{in} = \frac{w_i T}{4\pi R_s^2}$, where w_i is the width of the X-ray beam in the plane of the paper, T is the width of the beam in the in-and-out paper direction, and R_s is the distance between the X-ray source and the circuit board.
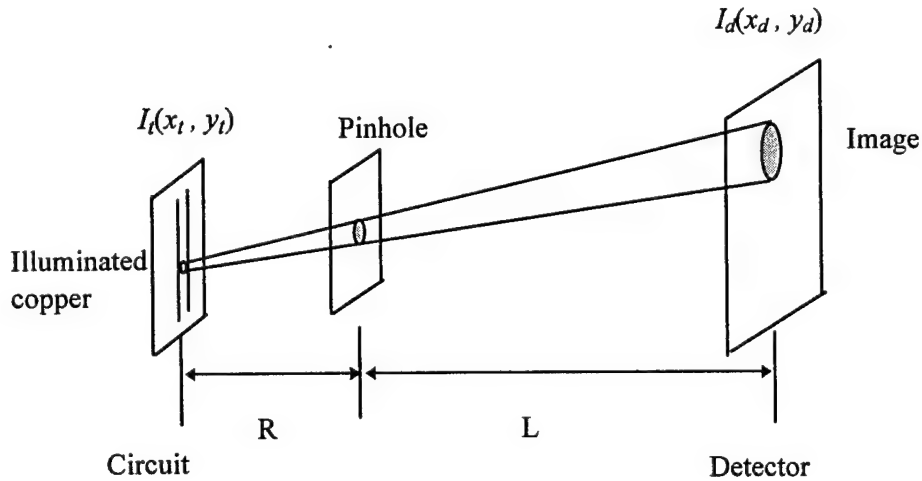

Figure 6. Resolution of the Circuit Board Image Through a Pinhole on the Detector Plane

4.2.2 Geometric Constraints on and Determination of the Design Parameters for the Pinhole Camera

Figure 7 illustrates the formation of an image of two copper traces in different layers by a pinhole camera on the detector plane. (Due to the short wavelength of the X-ray, no diffraction is considered.) Clearly, as long as $\theta_1 \leq \theta_2$, the two traces will eventually separate. The detector can be so arranged to collect photons that are scattered off one copper trace only.

From Figure 7, we have the following relations:

$$w'_i = w_i \cos\theta \text{, and}$$
$$w'_s = w_s \cos\theta,$$

where w'_i is the projection toward the path of the scattered X-ray, w_s is the width of the pinhole, and w'_s is the projection toward the scattered X-ray path.

The total flux is proportional to the product of these two projected areas and inversely proportional to the square of the distance between them. We have:

$$\varphi_{in}\frac{\Omega}{4\pi} = \frac{w'_i \, w'_s \, T^2}{16\pi^2 R_s^2 ((\frac{d+t}{2}+R)^2 + (\frac{w_s}{2}+D)^2)} t , \tag{10}$$

where d is the spacing between the copper traces, t is the thickness of the copper trace, R is the distance between the copper trace and the pinhole plane, and D the distance from the pinhole to the X-ray beam.

To separate the two traces, we must have $\theta_1 \leq \theta_2$. To simplify the argument, let $\theta_1 = \theta_2 = \theta$. Furthermore, the sum of the projected width of the pinhole and that of the copper trace should be less than the projected spacing:

$$w_i \cos\theta + t\sin\theta + w_s\cos\theta = d\sin\theta$$
$$(w_i + w_s) = (d - t)\tan\theta . \tag{11}$$

In practice, the distance R and D is much greater than the spacing and the thickness of the copper trace. We have, then, $R \gg \frac{d+t}{2}$, and $D \gg \frac{w_s}{2}$, with the relation $D = R\tan\theta$. Equation (10) is simplified to:

$$\varphi_{in}\frac{\Omega}{4\pi} = \frac{w_i w_s T^2}{16\pi^2 R_s^2 R^2}\cos 4\theta t . \tag{12}$$

Furthermore, we can determine the optimal conditions for w_s and w_i at a given angle. Using Equations (11) and (12), we have:

$$w_s = w_i = \frac{1}{2}(d - t)\tan\theta \tag{13}$$

Equation (12) becomes:

$$\varphi_{in}\frac{\Omega}{4\pi} = \frac{(d-t)^4}{64\pi^2 R_s^2 R^2}\sin^2\theta\cos^2\theta t \tag{14}$$

In Equation (14), T is taken to be the same as w_i. It follows from Equation (14) immediately that the closer the X-ray source to the circuit board and the closer the circuit board to the pinhole, the more flux received by the detector. The optimization condition for Equation (11) is reached when $\theta = 45^0$. For spacing = 122 microns (0.005 inch) and copper trace = 25 microns (0.001 inch), we have, from Equation (13), $w_i = w_s = 50\,\mu m$.

4.2.2.1 Optimization with absorption

In the above analysis we have ignored the absorption of the circuit board after the X-ray has been scattered. To take it into account, the absorption term in Equation (4) needs to be included:

$$\varphi_{out} \propto \frac{(d-t)^4}{64\pi^2 R_s^2 R^2}\sin^2\theta\cos^2\theta\exp(-\frac{\mu l}{\cos\theta})t, \tag{15}$$

where μ is the effective linear absorption coefficient of the circuit board (for example, mixture ratio of copper to G10 = 1:4), l is the path length in the circuit board of the X-ray after being scatted, and μ is a function of energy. Figures 8 and 9 show the energy dependence of μ of copper and G10.

Equation (15) has to be numerically solved in order to find the optimal condition. Figures 10 and 11 show the intensity and its first derivative of Equation (15). At 160 KeV, the product of μl is in the order of 0.1, and has very little effect on the optimization condition. At 40 KeV, μl is approximately 0.88, the optimal angle reduced to 38 degree. Table 1 lists the optimal angle and widths for several energies.

Table 1. Optimization Conditions for Pinhole Camera with Absorption

Energy (KeV)	μl	Attenuation (%)	θ (degree)	w_i (μm)	w_s (μm)
160	0.09	8.7	45	20	50
80	0.20	18	43	47	47
40	0.88	59	38	40	40

4.2.2.2 Global optimization

A global optimization can be obtained by combining Equations (15) into (4), which includes both geometric constraints of this section and the kinematic and electrodynamic constrains of first section:

$$\varphi_{out} = \frac{(d-t)^4}{64\pi^2 R_s^2 R^2}\sin^2\theta\cos^2\theta\exp(-\frac{\mu l}{\cos\theta})\sigma(\theta)t. \tag{16}$$

Optimal conditions are numerically obtained (see Figures 12 and 13) for energy level 40, 80, and 160 KeV, and listed in Table 2.

Table 2. Global Optimization Conditions for Pinhole Camera

Energy (KeV)	μl	Attenuation (%)	θ (degree)	w_i (μm)	w_s (μm)
160	0.09	8.7	38	40	40
80	0.20	18	37	38	38
40	0.88	59	34	34	34

4.2.3 Geometric Constraints on and Determination of the Design Parameters for the Ring-Slit Camera

4.2.3.1 General consideration

The distribution of the Compton scattered photons is symmetric about the incident X-ray beam. Taking advantage of this symmetry, we can design a ring slit in place of the pinhole to increase the total photon flux. In this case Equation (10) becomes:

$$\varphi_{in} \frac{\Omega}{4\pi} = \frac{2\pi(\frac{w_s}{2} + D)w_i'^2 w_s'}{16\pi^2 R_s^2 ((\frac{d+t}{2} + R)^2 + (\frac{w_s}{2} + D)^2)} t . \tag{17}$$

with the conditions $R \gg \frac{d+t}{2}, D \gg \frac{w_s}{2}$, and the relation $D = R\tan\theta$. Using Equations (11) and (16) we have:

$$w_i = 2w_s = \frac{2}{3}(d-t)\tan\theta \tag{18}$$

$$\varphi_{out} = \frac{(d-t)^3}{27\pi R_s^2 R}\sin^3\theta\cos\,\theta t . \tag{19}$$

Equation (19) reaches maximal at $\theta = 60^0$. Equation (18) gives, at $\theta = 60^0$, $w_i = 2w_s = 58\,\mu$m .

Compared with the optimization for a pinhole, there are several noticeable differences for the ring slit. First, the flux depends linearly on the inverse of the distance between the circuit board and the slit; this is because the circumference of the ring slit is proportional to the distance. Second, the optimal width for the beam is different from that of the slit; this is caused by the different power dependence of the flux on the two widths.
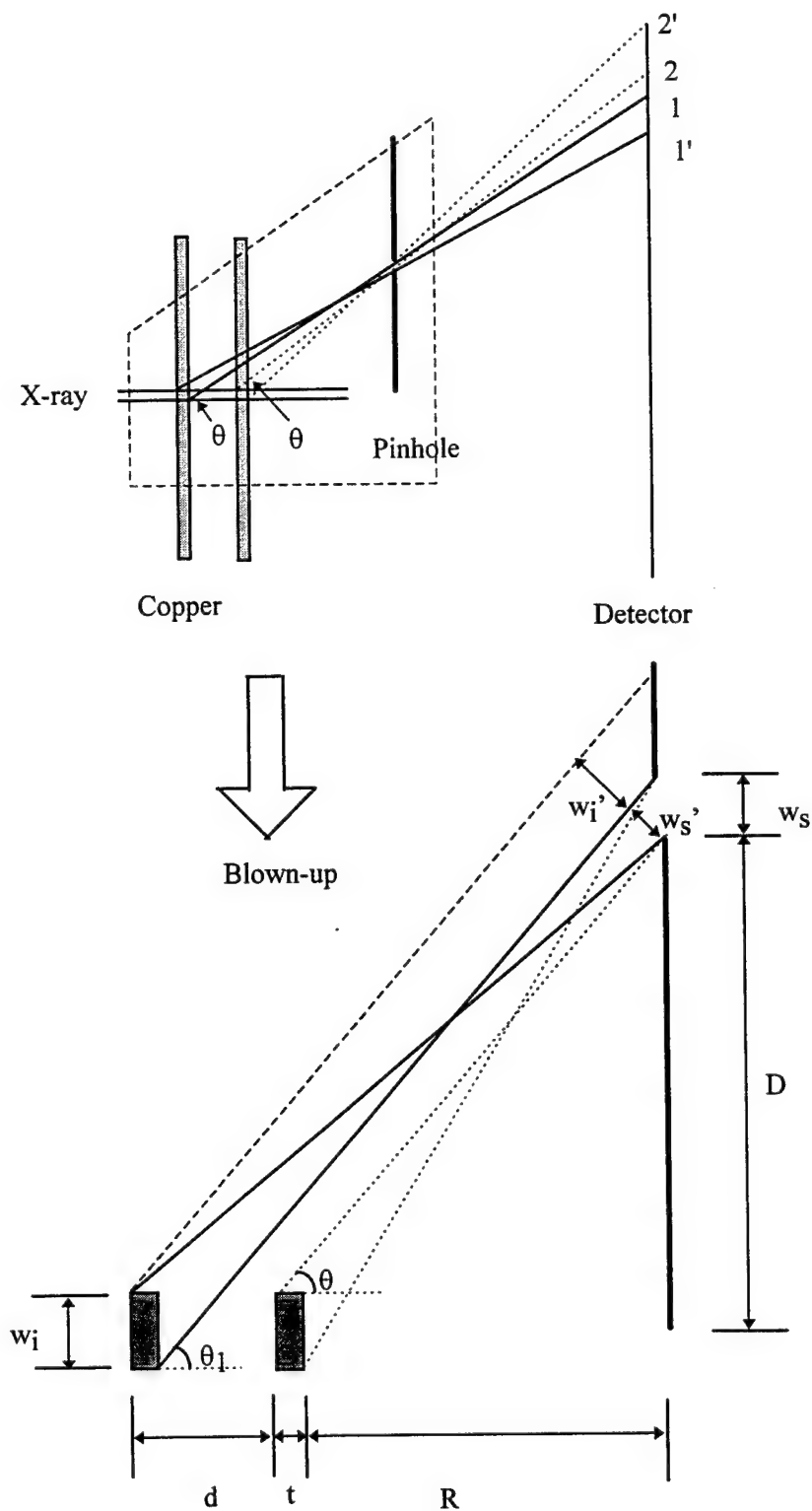
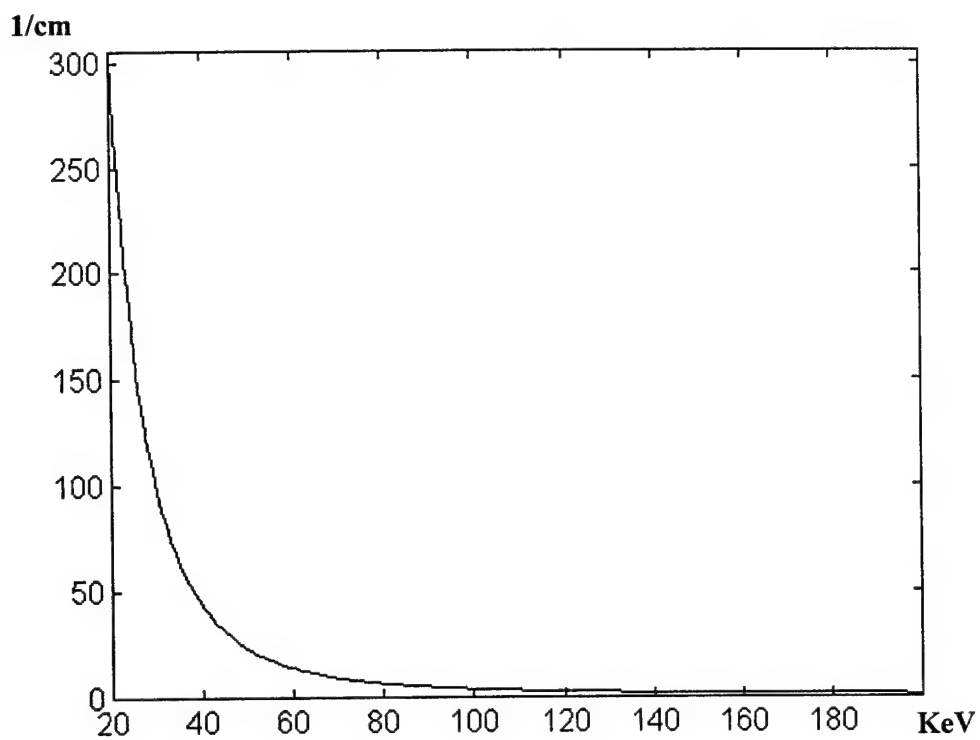**Figure 7. Image of the Copper Traces Through a Pinhole Camera**

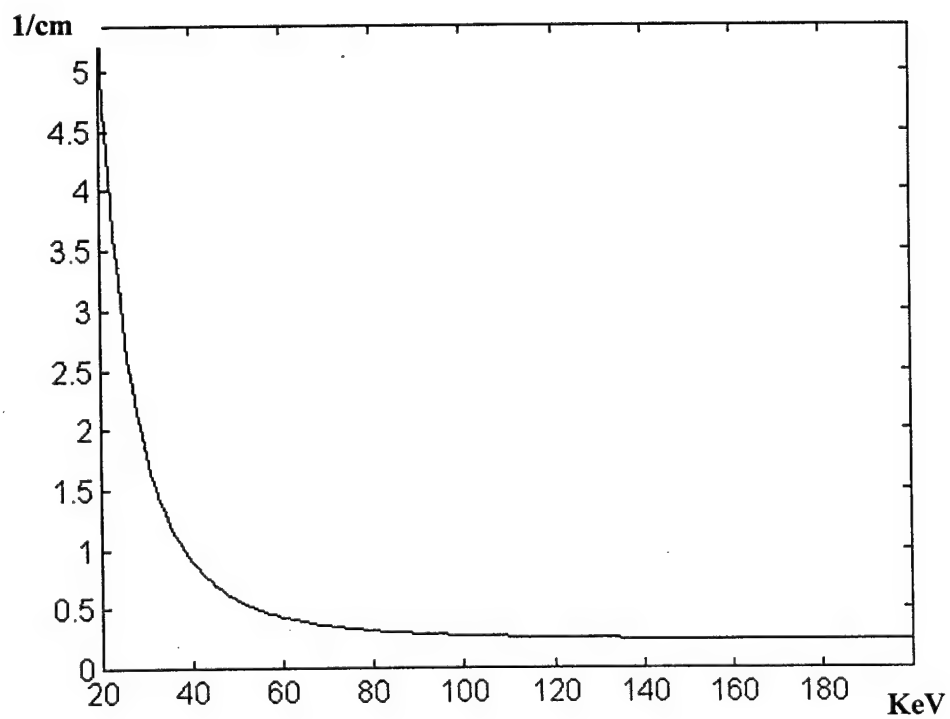**Figure 8. Total Linear Attenuation of Cu**

Figure 9. Total Linear Attenuation of G10
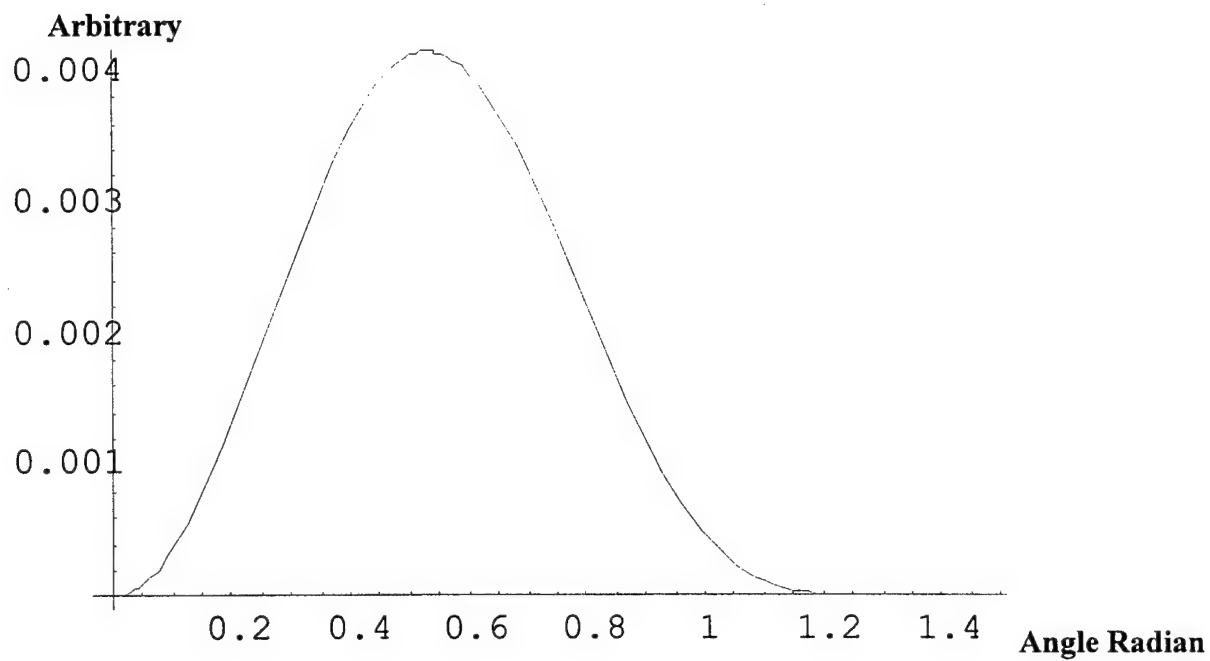
Figure 10. Plot of Equation (14)
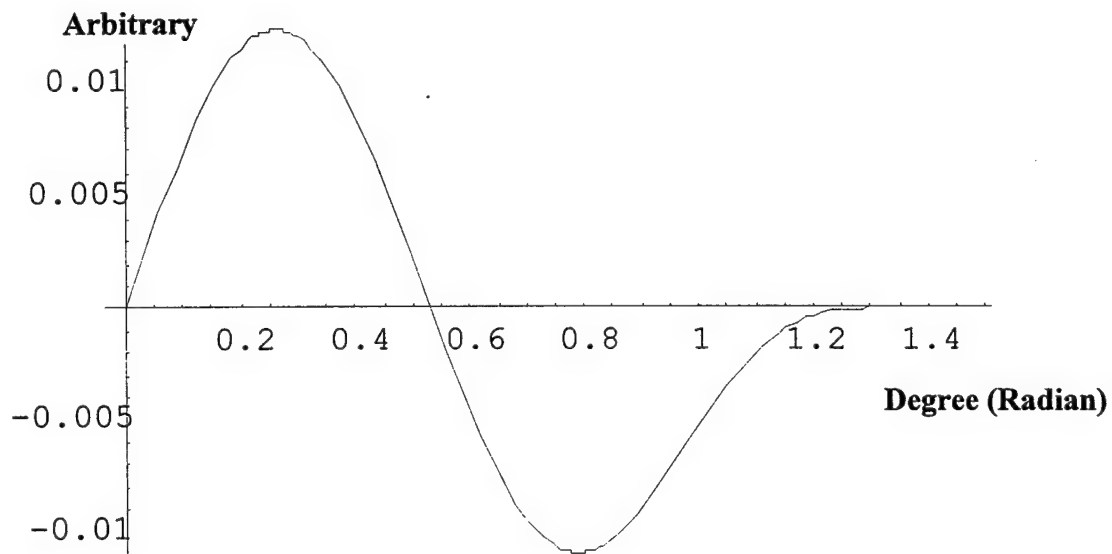
Figure 11. First Derivative of Equation (14)

Arbitrary

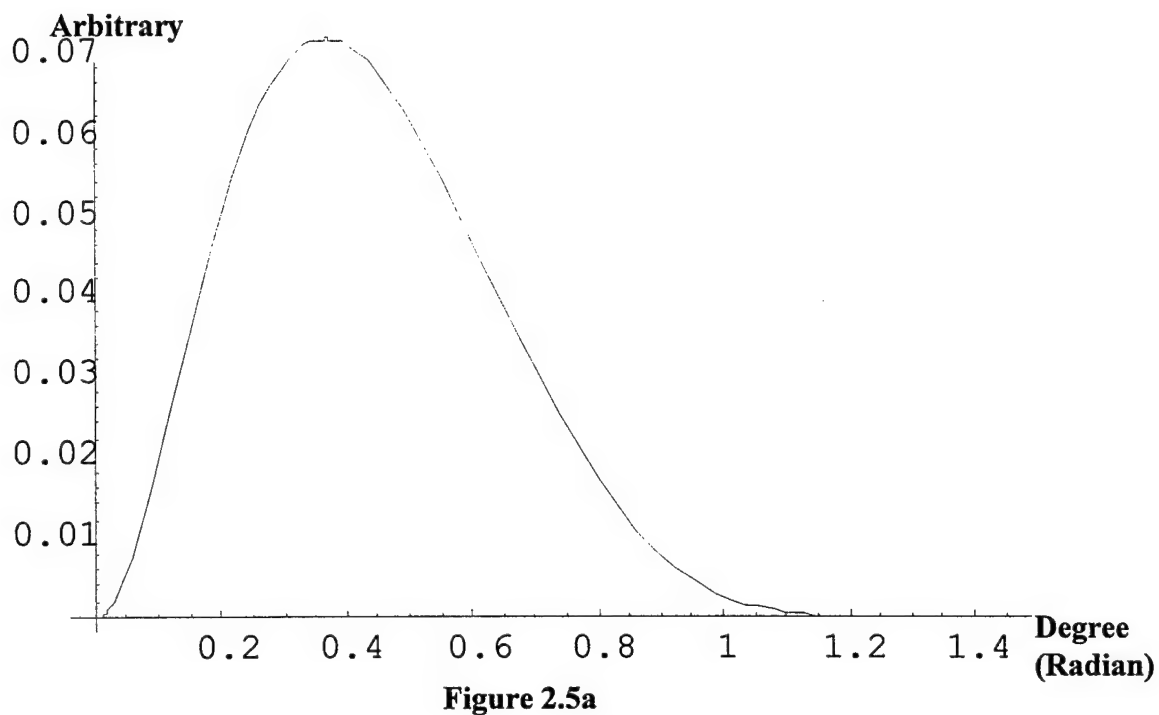
Figure 2.5a

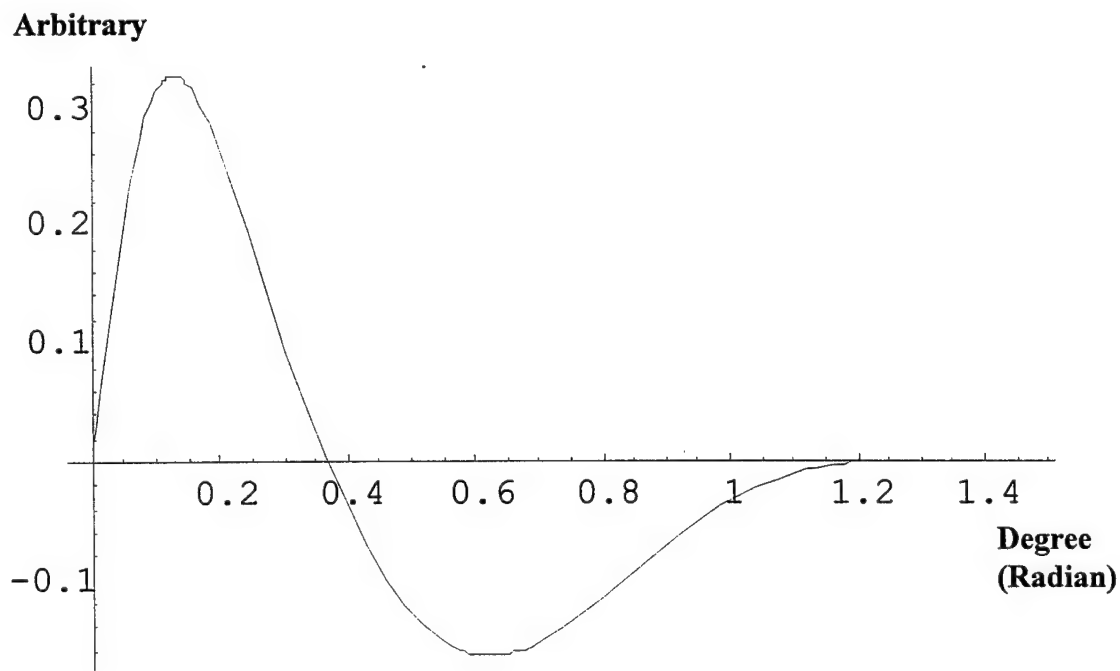**Figure 12. Plot of Equation (15)**

Arbitrary

Figure 13. First Derivative of Equation (15)

4.2.3.2 Optimization with absorption

With absorption, Equation (19) becomes:

$$\varphi_{out} \propto \frac{(d-t)^3}{27\pi R_s^2 R} \sin^3 \theta \cos \theta \exp(-\frac{\mu l}{\cos \theta})t \ . \tag{20}$$

Optimization conditions can be numerically determined (see Figure 14 and 15). They are calculated and listed in Table 3 for 40, 80, and 160 KeV.

Table 3. Optimization Conditions for Ring-Slit Camera with Absorption

Energy (KeV)	μl	Attenuation (%)	θ (degree)	w_i (μm)	w_s (μm)
160	0.09	8.7	57	104	52
80	0.20	18	56	100	50
40	0.88	59	48	75	38

4.2.3.3 Global optimization

Global optimal conditions are obtained by substituting Equation (20) into (4) and solving numerically the following equation (see Figures 16 and 17):

$$\varphi_{out} \propto \frac{(d-t)^4}{27\pi R} \sin^3 \theta \cos \theta \exp(-\frac{\mu l}{\cos \theta})\sigma(\theta)t \ . \tag{21}$$

The results are listed in Table 4 for 40, 80, and 160 KeV.

Table 4. Global Optimization Conditions for Ring-Slit Camera

Energy (KeV)	μl	Attenuation (%)	θ (degree)	w_i (μm)	w_s (μm)
160	0.09	8.7	51	84	42
80	0.20	18	50	81	40
40	0.88	59	44	66	33

Figure 2.6a

Figure 14. Plot of Equation (19)

Figure 15. First Derivative of Equation (19)
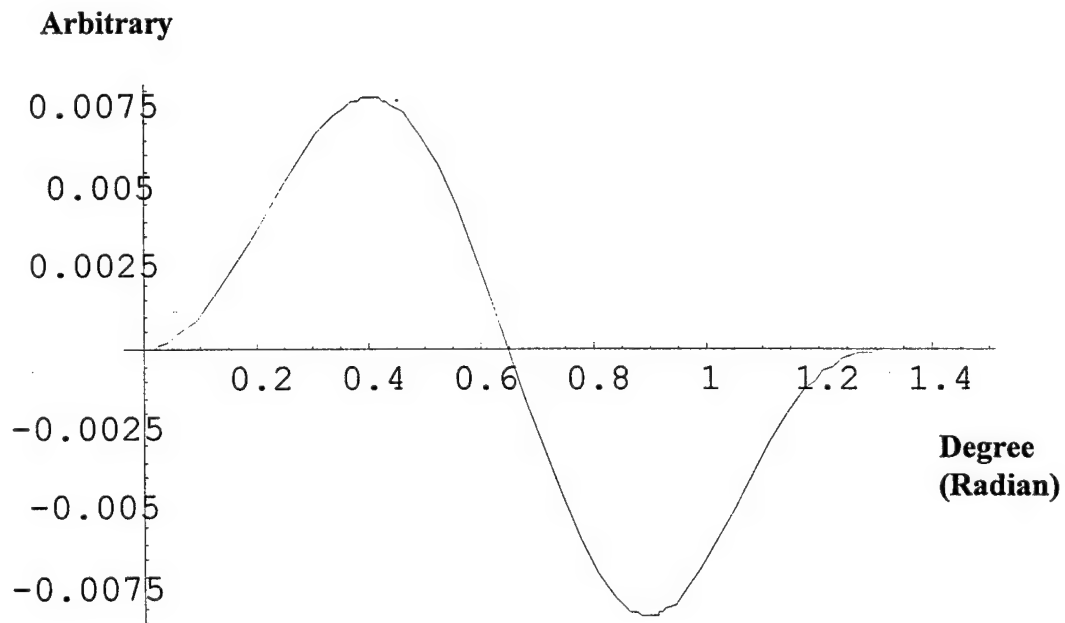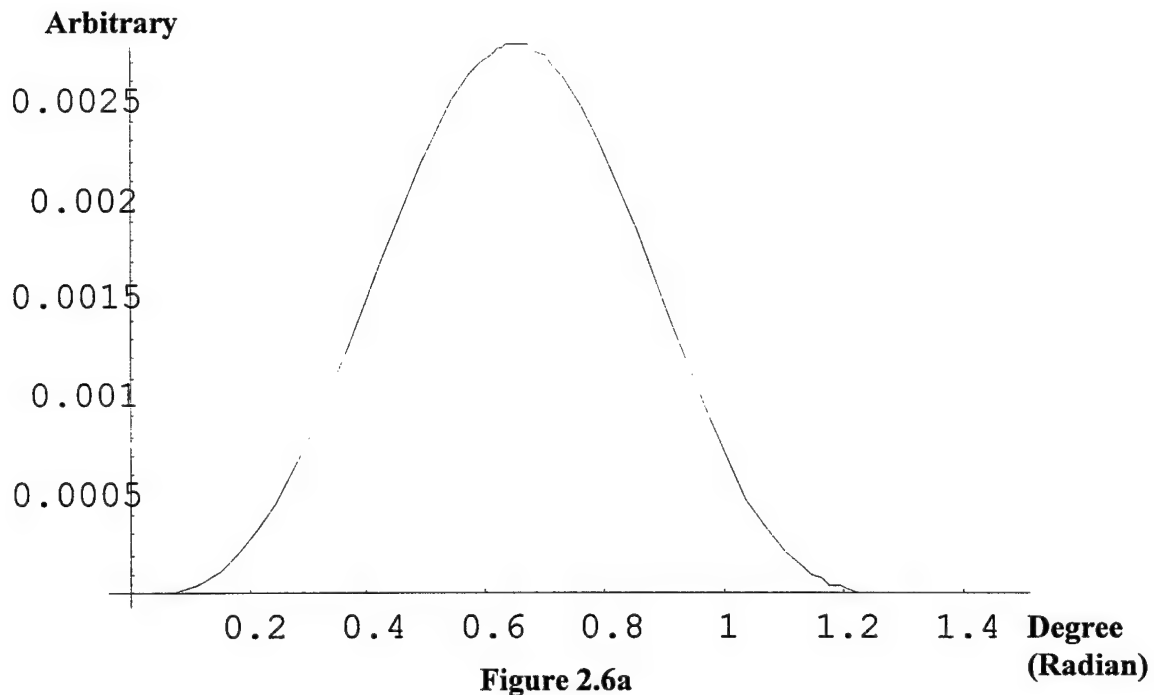
Figaure 2.7a

Figure 16. Plot of Equation (20)

Figure 17. First Derivative of Equation (20)

4.2.4 Resolution of the System

Note that the optimal conditions derived above are based on Equations (16) and (21). The resolution is determined by the condition $\theta_1 \leq \theta_2$. The image of the copper traces on the detector plane is the convolution of the traces and the pinhole. With the equality sign, the images of two traces always overlap by w_S, the width of the slit. The separa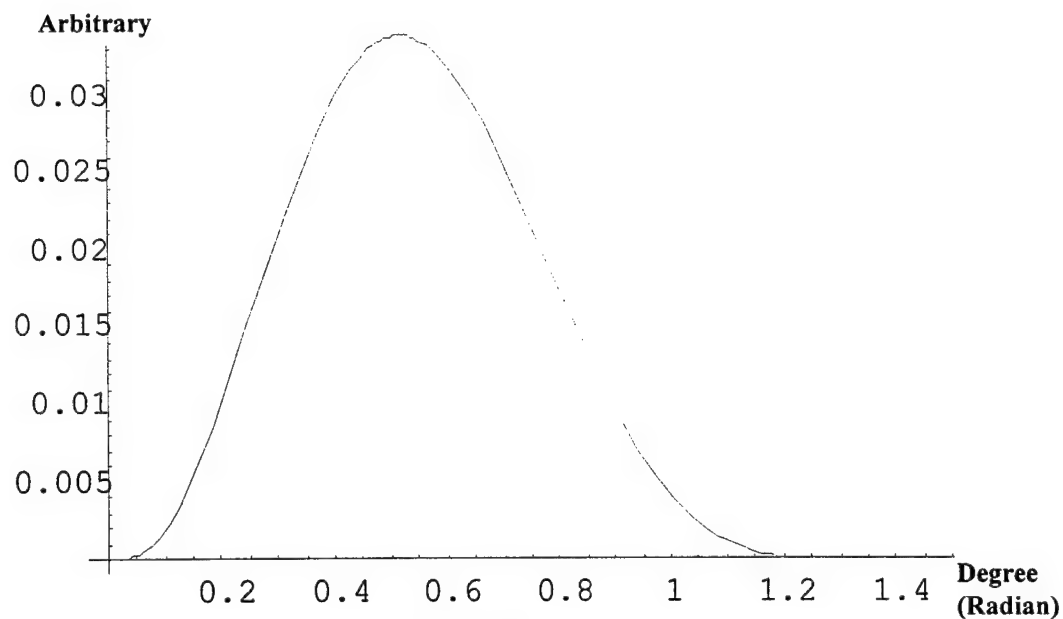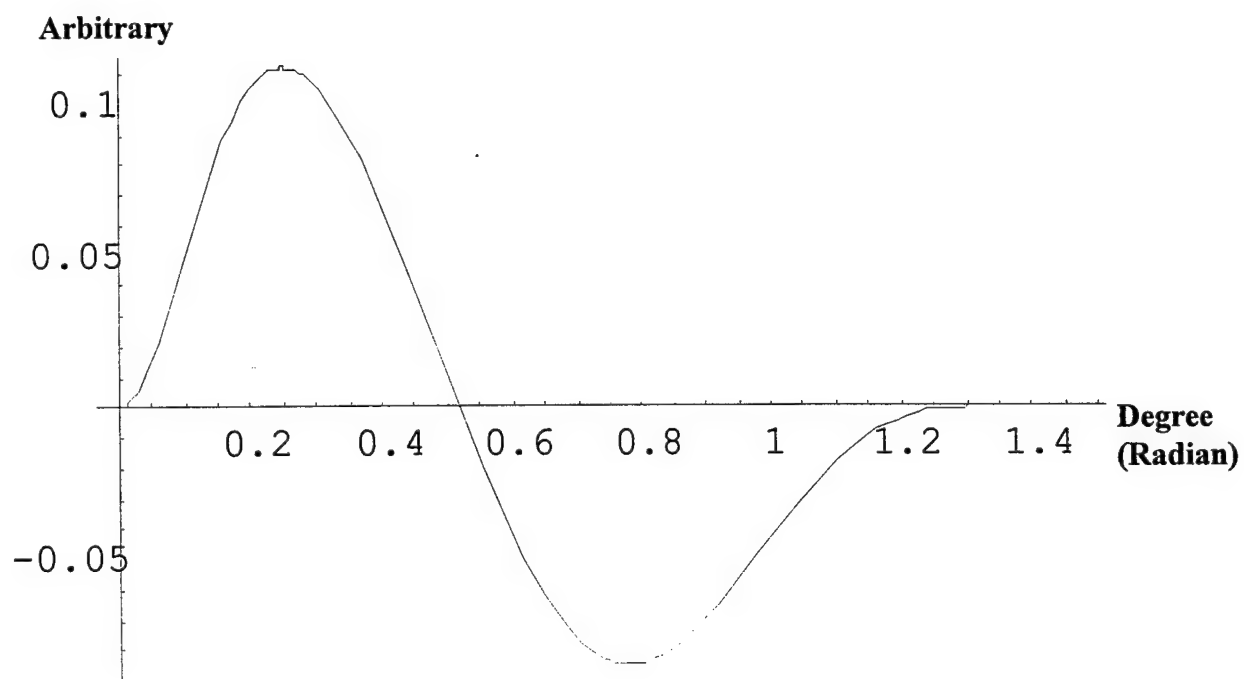tion of the two peaks (the resolution) produced by the pinhole (or the ring slit) depends on the position of the detector plane. In Figure 18, images of two adjacent copper traces on the detector planes are illustrated. The numbers correspond to the rays in Figure 7. The further away the detector plane is from the pinhole (or the ring slit), the higher the system resolution. Total separation can be easily achieved by making either the beam width or the slit width smaller than those given by the optimal conditions. For example, take the beam width to be one half of those determined by the optimization conditions, separations between ray 1-2 and 1'-2' in the unit of w_s as a function of the position of the detector plane is plotted in Figure 19. The distance between the circuit board and the slit is assumed to be 5 mm with a copper trace spacing between layers of 100 microns.
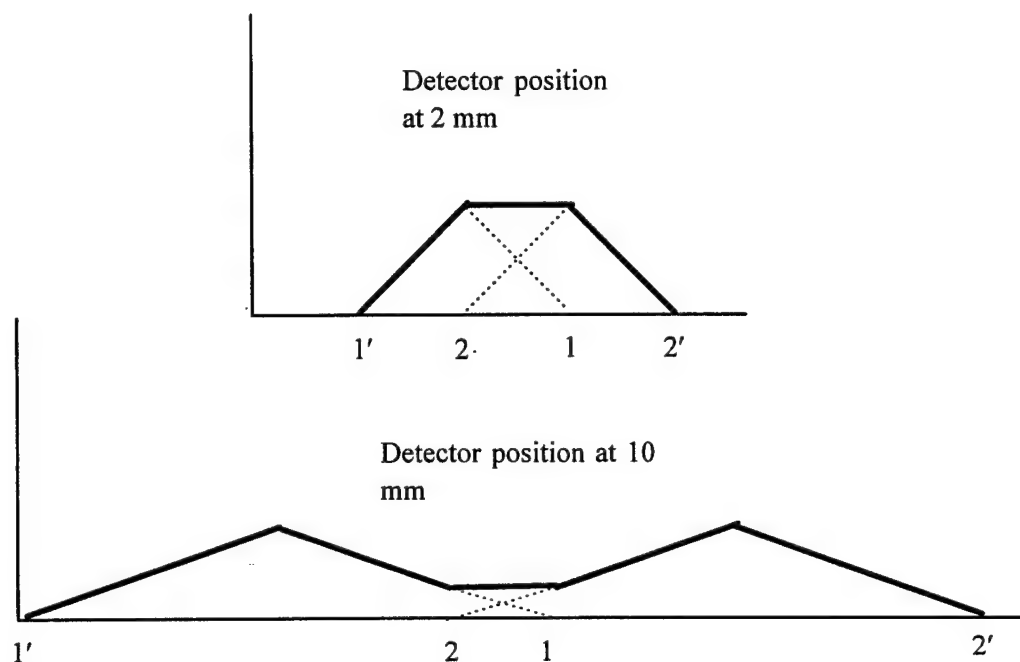

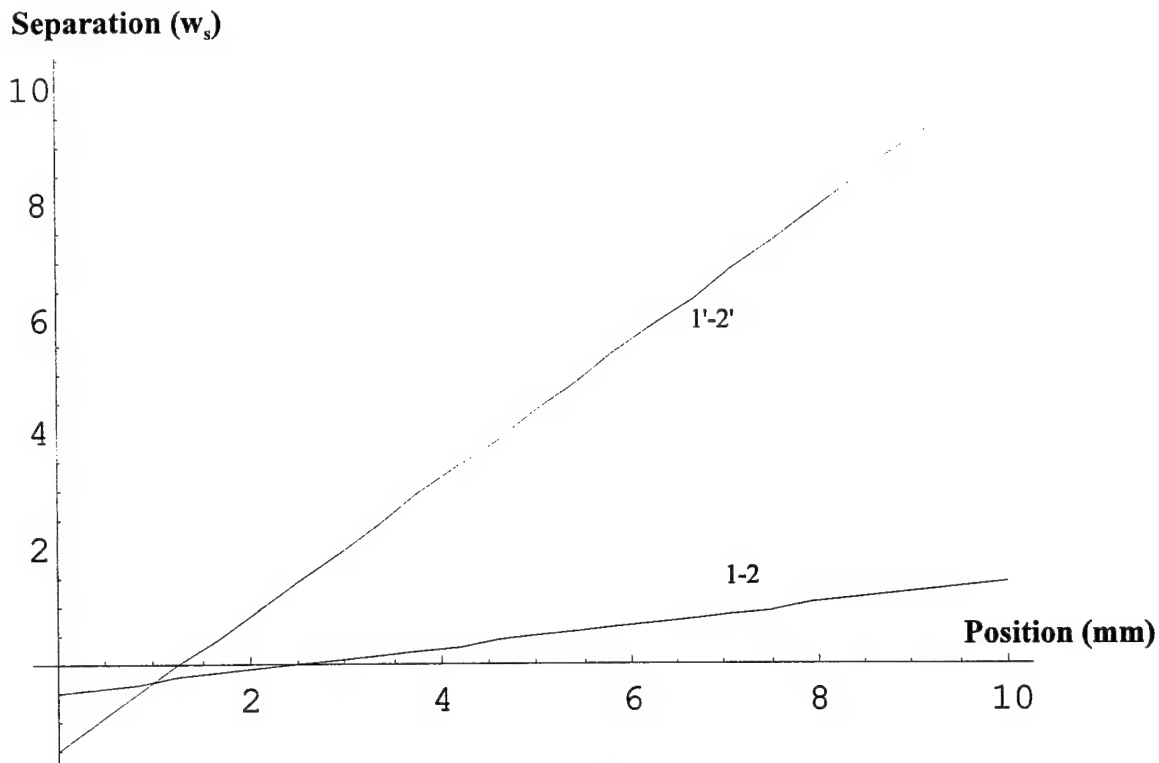**Figure 18. Adjacent Copper Traces on the Detector Planes**

Figure 2.9

Figure 19. Ray Separations as a Function of the Position of the Detector Plane

4.2.5 System Efficiency

The efficiency of the system is defined here as the product of the two solid angles (the X-ray source to the copper trace and the copper trace to the detector), which is given by Equation (9). For a given resolution, it can be calculated using Equations (15) and (20).

For spacing of 100 μm and 25 μm thick copper, the efficiency is:

- For a pinhole camera with the circuit board placed 5 mm away from the circuit board and the circuit board 5 mm away from the camera, system efficiency ~ $10^{-12} \sim 10^{-11}$.

- For a ring-slit camera with the circuit board placed 5 mm away from the circuit board and the circuit board 5 mm away from the camera, system efficiency ~ $10^{-9} \sim 10^{-8}$.

The ring-slit camera's efficiency is more than three orders of magnitude higher than that of the pinhole camera. The total photons received by the detector can be calculated for a given X-ray source using Equation (19).

For example a FeinFocus micro-focus X-ray tube has a power density of about 1 watt per square micron with a total wattage of about 10 watts. If only 1 percent of the input power is converted to X-ray energy, at 200 KeV, there will be roughly 10^{13} - 10^{14} X-ray photons generated in a 2π solid angle. For a copper trace of 25 μm thick, the X-ray photon received by the pinhole detector is less than 1 photon per second and for a ring-slit camera, the photon received is about 10^2 - 10^3.

For a synchrotron source, for a collimated beam of the same diameter, the photon flux is at least 6 orders of magnitude higher. That is $10^5 \sim 10^6$ photons per second for a pinhole detector and $10^8 \sim 10^9$ for a ring-slit camera.

4.2.6 Collimator

So far we have assumed that the X-ray is a pencil beam. However, most X-rays are generated in a 2π solid angle. So to achieve a pencil beam a collimator has to be placed in front of the X-ray tube.

As shown in Figure 20, the attenuated X-ray beam has to be at least two orders of magnitude smaller than that scattered by the copper trace. The intensity of Compton scattered radiation in the unit of photons per unit solid angle is about 10^{-4} smaller than that generated by the X-ray tube, assuming the copper trace is 25 μm thick and 5 mm away from the X-ray. This means the attenuated radiation has to be at least a few orders of magnitude smaller than 10^{-4}. A 2-mm-thick tungsten plate will attenuate X-ray radiation at 100 KeV by a factor of $4*10^{-8}$. A 2-mm-thick Pb plate will attenuate X-ray radiation at 100 KeV by a factor of $4*10^{-6}$.

Geometrically, the diameter of the collimator has to be small enough such that the beam diameter at the copper trace of interest be less than that required by the optimal conditions. To produce a 50 μm in diameter beam at a copper trace 5 mm away from the X-ray target, a pinhole of 25 μm in diameter in a 1-mm tungsten plate placed 2.5 mm in front of the copper trace will serve these requirements.

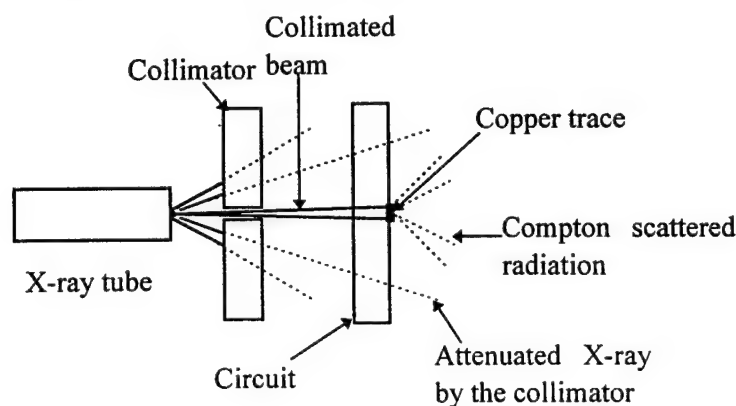**Figure 20. Collimator**

4.2.7 Conclusions

- The source and detector should be at opposite sides of the circuit board.
- The circuit board should be placed as close to the X-ray source as possible.
- A pinhole (or slit) should be placed as close to the circuit board as possible.
- System efficiency for ring-slit camera is more than three orders of magnitude higher than that of the pinhole camera.

- The optimization condition for a pinhole camera is when it is placed at about 34 degrees from the incident beam, and for a ring-slit camera, the optimal condition is reached when the slit is positioned at 44 degrees.

- A collimator made of 1-mm tungsten plate is preferred.

4.3 Task 3. System Designs and Construction

4.3.1 Pinhole Camera with a Point Detector

A schematic diagram of the pinhole camera is shown in Figure 21.
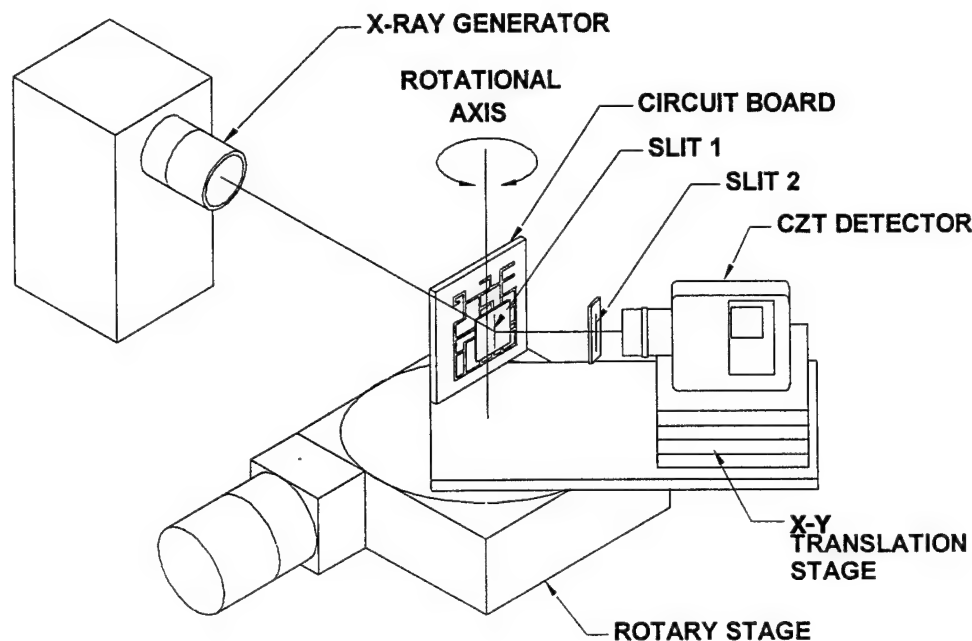
Figure 21. Schematic Diagram of the Pinhole Compton Detection System

An AmpTek XR-100T-CZT (CaZnTe) detector is used in the camera. This detector has a 2-mm detection area. An adjustable slit is made to fit in front of the detector window, the detection resolution therefore can be adjusted.

In place of a pinhole, an adjustable slit is made. The slit width can be adjusted continuously from 25 microns to 2.5 microns. The slit and the CZT detector are mounted on an x-y translation stage. This translation stage is then mounted on a rotary stage, so it can detect the scattering at different angles.

The circuit board is held with a circuit board holder normal to the incident beam with the rotational axis going through it. As the detector rotates, the scattered radiation off the circuit board always maintains at the center of rotation of the detector.

The CZT detector can be translated along and perpendicular to the scattering angle. By translating it along the scattering angle, the system resolution can be adjusted, and perpendicular to it, the scattering from copper trace of different layers can be detected (see Figure 26).

4.3.2 Ring-Slit Camera with a Scintillation Detector

Figure 22 shows the cross section of the ring-slit camera. The ring-slit detector head consists of a set of tungsten masks, a NaI scintillation crystal coupled with an A2 PM tube and mechanical, optical distance and displacement gages, and a Si array detector.

The distance between the circuit board and the surface of the slit mask assembly is 5 mm. This number is determined by consideration that it cover the thickness of most circuit boards including one that has 30 layers with 100 μm spacing.
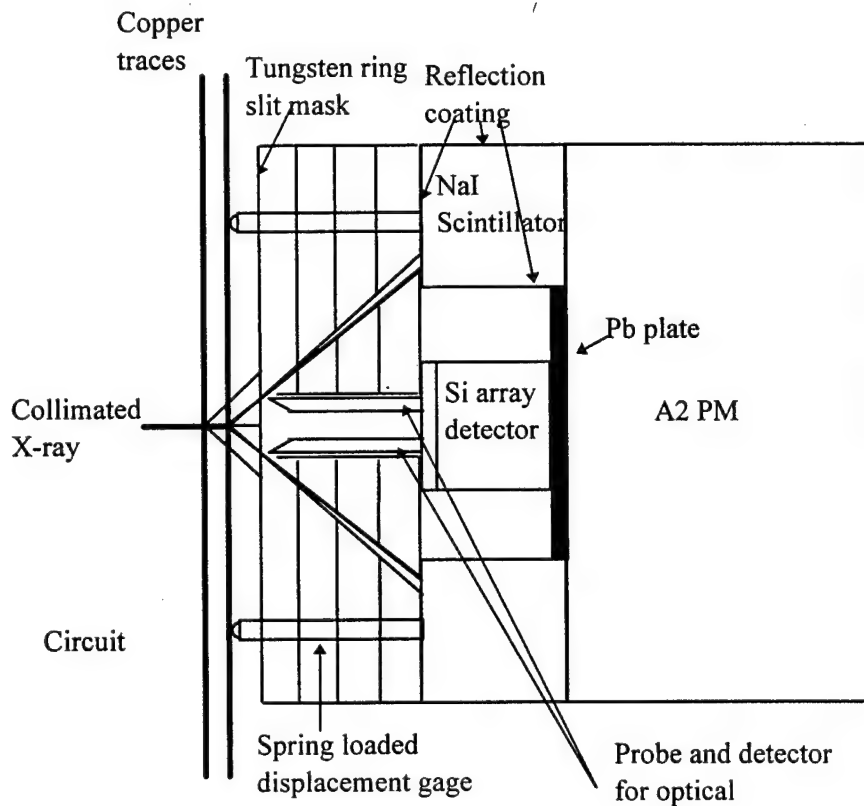
Figure 22. Cross Section of the Ring-Slit Detection System

The slit width of each mask is defined by ray 1-1' of Figure 7 and can be found from Figure 19. The total thickness of the tungsten mask assembly is 10. As shown in Figure 19, at about 10 mm, the separation between ray 1-2 of Figure 7 is about 2 w_s and that between ray 1'-2' is 10 w_s [w_s is the width of the slit determined by the optimal condition using Equation (20)]. This means that the separation between the peaks is about 2/3 of the width of the peaks.

The different layers are brought into the field of view of the slit camera by varying the distance between the circuit board and the detector head. The depth of each copper layer is determined by detecting variations of the scattered radiation. There is a one-to-one correspondence between the displacement of the head and the separation between the layers.

The detected radiation intensity as the head moves can be considered as the convolution of the last slit and the image in Figure 18. With the separation indicated above, even if the image is a step function, an outstanding resolution can be achieve.

Three spring-loaded mechanical displacement gages and QUEST's proprietary optical triangulation probe is used for both distance and displacement measurements. The optical triangulation probe is an excellent tool for measuring the absolute distance between the head and the circuit board. This will remove the errors introduced by any deformation of the circuit board, since this optical probe measures the same area where the incident beam going through. Another advantage of using optical triangulation is that it can distinguish between different surfaces (different reflection characters) such as copper traces, circuit board substrate, and a through hole or a via (no reflection). The reason to use three mechanical-displacement gages is that for a reasonably large circuit board, as the head moves to one edge of it, there will always be one on the board.

NaI scintillator coupled with low-noise A2 photo-multiplier is used as the detector. NaI has very high conversion efficiency. At 500 KeV, for a 13-mm thick NaI crystal, 99% of the X-ray photons will be attenuated and most of them will be converted to visible photons. The NaI crystal is sealed with $25\,\mu m$ thick Al reflection layer. So all the visible photons created in the crystal will be eventually couple into the MP tube. The A2 PM tube has very low dark current, it is capable of detecting single photons.

An Si array detector is used both for 2-D projection detection and centering the detection head with respect to the incident beam. To increase the detection sensitivity of the Si array detector, a thin layer of scintillating material can be applied to the surface of it.

There is a Pb plate underneath the Si array detector and its preamp. This plate is about 2-mm thick and will attenuate any stray radiation or transmitted X-ray photons by a factor of 10^{-15}.

Figures 23 and 24 show the assembly of the system schematically, and the method it uses to scan the circuit board.

4.4 Task 4. Data Acquisition and Experimental Results

Two experiments were conducted to verify the model developed in Task 1 and the design parameters established in Task 2. First experiment was carried out using the ring camera with a CZT detector. The scattering efficiency of sample materials was tested. The second experiment was conducted with the ring-slit camera. It was shown that the copper structure at different depths could be detected.
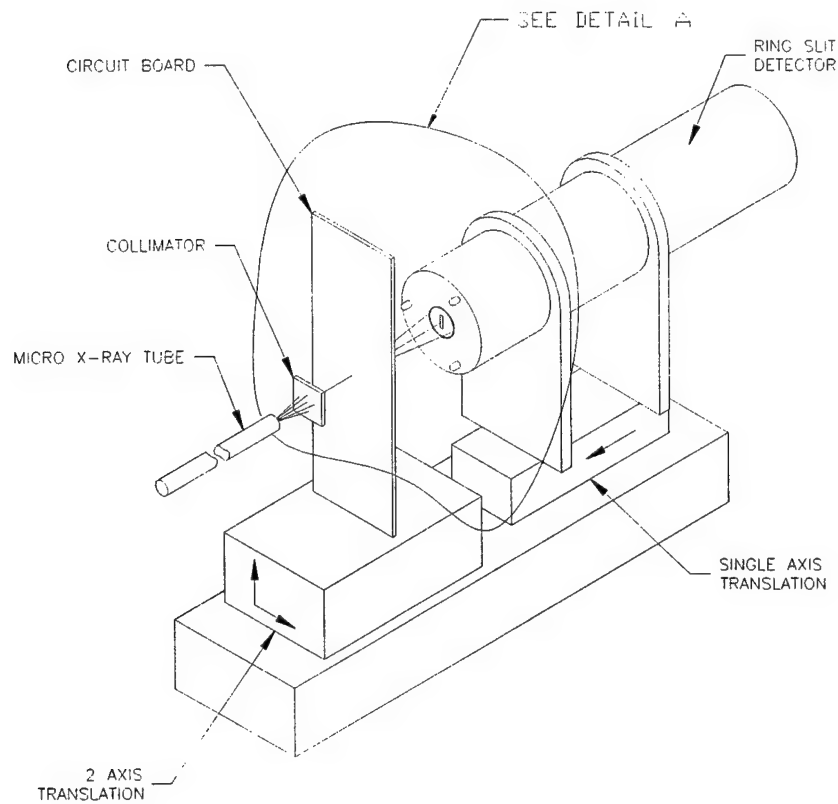
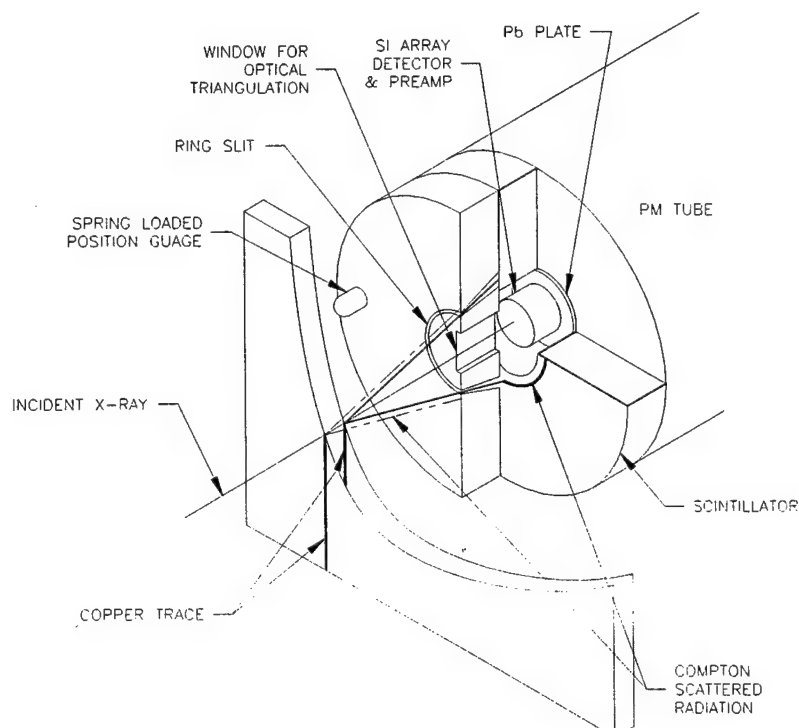**Figure 23. Schematic Diagram of the Ring-Slit Compton Scattering Detection System**

Figure 24. Detail of "A" in Figure 23

4.4.1 Test Sample

A 1.5 mm G10 board was used to evaluate the efficiency of the system. The samples used for investigating variation of the scattered radiation intensity included: G10 (plain board) and the circuit board 6934485, 98747 BD, 6302341-1, 6302341-5, provided by the U.S. Air Force, and two dummy boards. The first dummy samples were constructed with G10 copper traces of different thickness. The second dummy board has two copper layers, 220 μm thick each separated by a 1.5 mm G10 substrate. This sample was used to evaluate the system depth resolution. The dimensions are shown in the diagram in Figure 25.
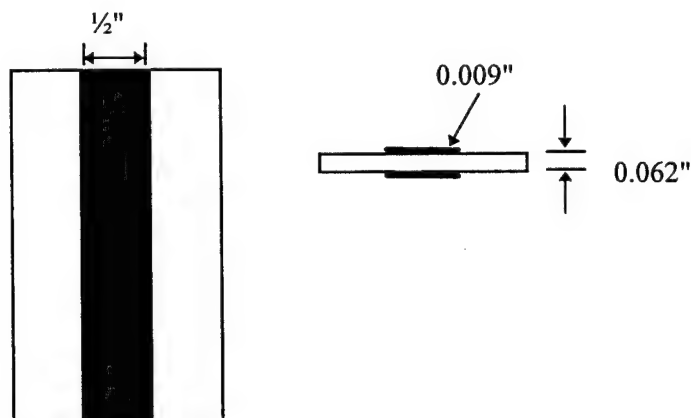

Figure 25. Prepared Multi-layer Circuit Board

4.4.2 Test Equipment

Table 5 describes the test equipment used in these experiments.

Table 5. Description of Test Equipment

Equipment	Description
X-ray generator	XRG 5000
X-ray generator	FeinFocus 160 KeV with 5-axis manipulator
pinhole camera	Constructed
Ring-slit camera	Constructed
X-ray detector	AmpTek CZT RX 100T S/N 01722
Scintillator	Rexon CsI 7653
Amplifier	AmpTek S/N 867
Scintillator power supply and amplifier	Rexon AP-2H
Multi-Channel Analyzer (MCA)	AmpTek 8000 S/N 001097
PC computer	Intel Pentium Pro

4.4.3 Test with Pinhole Camera

4.4.3.1 Experimental arrangement

Figure 26 shows the experimental arrangement. The circuit board is held above a rotary stage but is independent of the motion of the stage. The rotational axis goes through the point where the copper trace and the incident X-ray beam cross. The detector assembly consists of slit1, slit2 and the x-y translation stage. This assembly is attached to the rotary stage, so it can rotate about the circuit board and measure the Compton scattered radiation at different angles. The CZT detector can move both along the direction of the scattering and perpendicular to it. With proper slit widths of slit1 and slit2, the scattering from copper of different layer can be detected. Figure 27 is a photograph of the experimental setup.

Figure 28 shows the block diagram of the data acquisition process. The data acquisition is executed by running the multi-channel analyzer (MCA) control software on the PC. The signal is amplified and analyzed by the preamp, amplifier and MCA, and finally stored in the PC.

4.4.3.2 System efficiency

The number of photons expected from the X-ray source is in the order of 10^{14}. The efficiency of the system with the slit wide open, is about 10^{-11}. The photon expected at the detector is estimated at $4*10^3$. The measured value is on average $2*10^3$.

It is difficult to obtain a very accurate estimate on the number of photon scattered, because at low energy ranges, the X-rays are highly absorbed. Accurate calculation needs not only a complicated integral, but also more experimental data on X-ray. So we consider the measured value to be on the same order of magnitude as the estimated photon count.
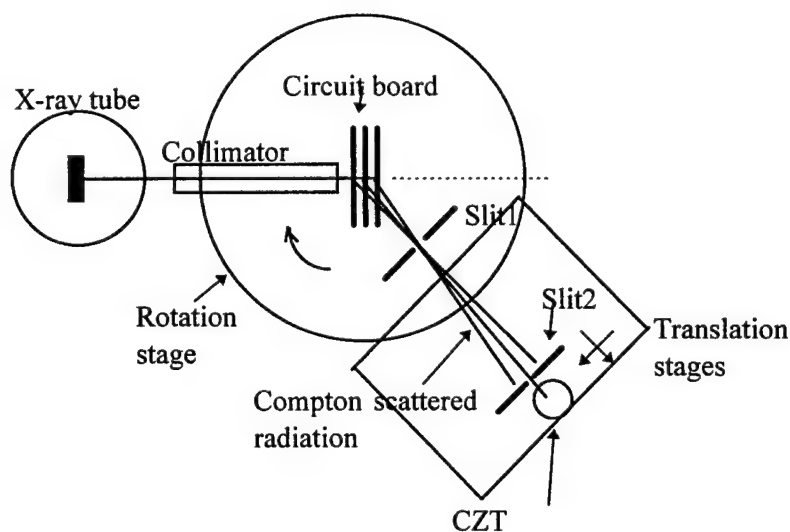

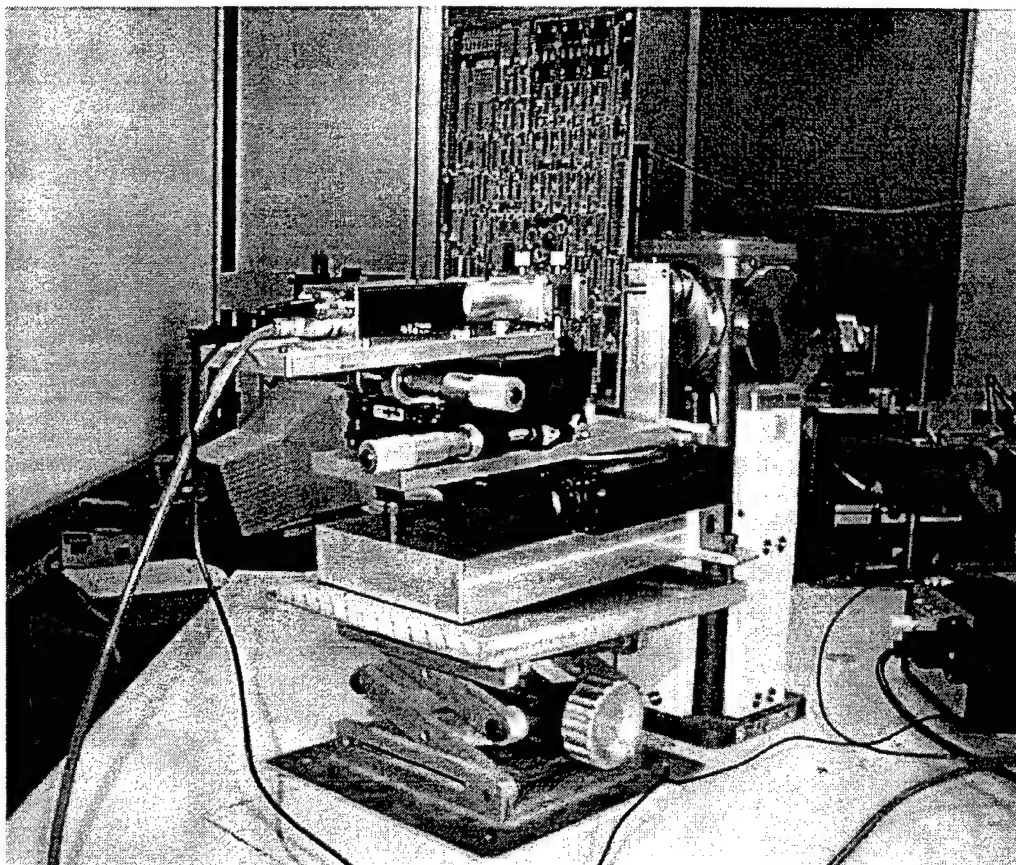**Figure 26. Experimental Arrangement**
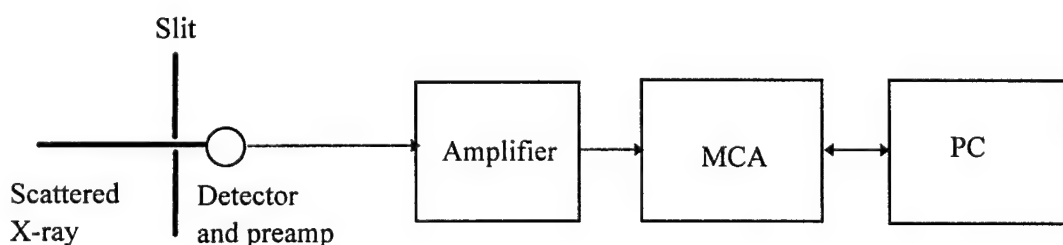
Figure 27. Photograph of the Experimental Arrangement

Figure 28. Block Diagram for Data Acquisition

4.4.3.3 Scattered intensities of substrate materials

The scattered intensities of various circuit board substrate materials have been investigated. They include G10, 6934485, 98747 BD, 6302341-1, and 6302341-5. Figure 29 shows one of the Compton scattered radiation data of copper trace on G10 substrate (it was collected with the slits wide open). There are several distinct peaks that can be identified with various materials in the X-ray path in the circuit board. They are marked in Figure 26. These peaks are, we believe, caused by the photoelectric effect. These characteristic peaks might be used to provide further information such as the presence of copper, etc. Further investigation is needed to quantify them.

It is concluded that there is no measurable difference in scattered photon intensities between G10 and 6934485, 6302341-1, and 6302341-5. However, we could not find a large enough place where there was no copper trace or ground plane to conduct this test reliably on 98747 BD. From this experiment, we concluded that the circuit board materials tested can be represented by G10. The test results are listed Table 6. The numbers in the brackets are the uncertainties.

Table 6. Test Results

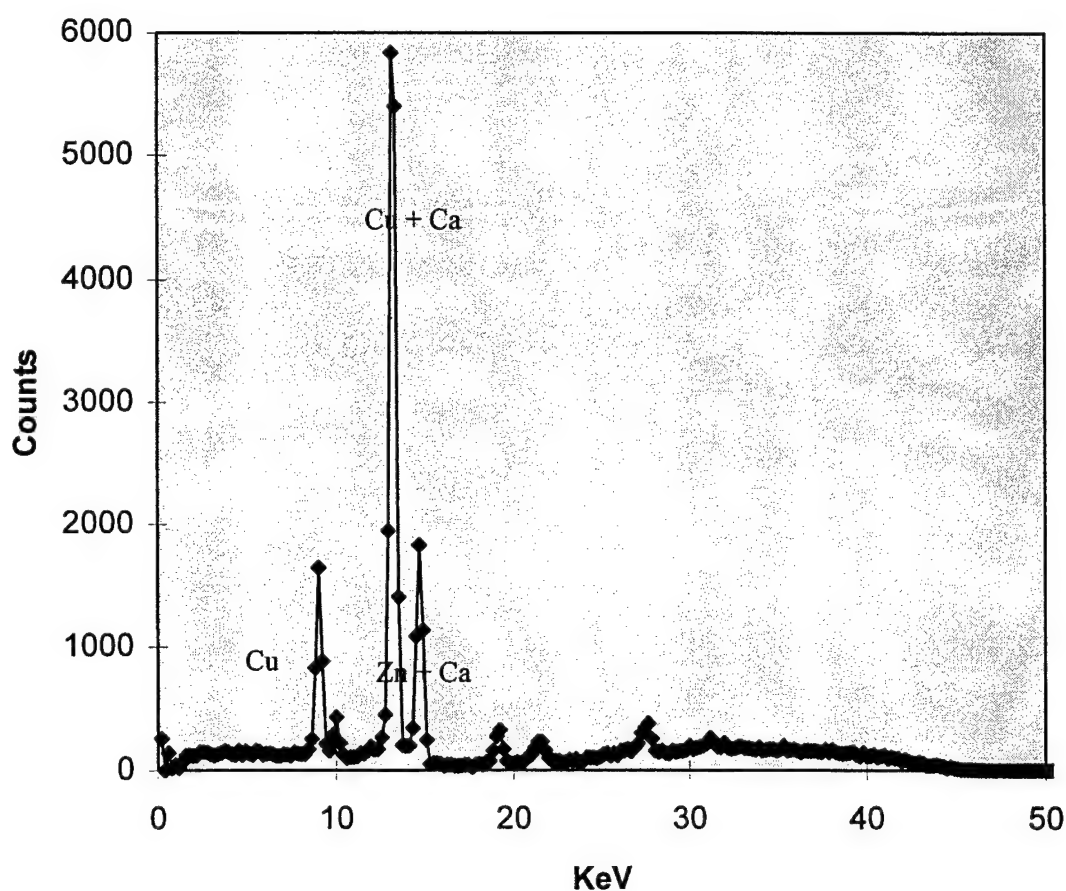| Circuit board ID	Photon count per second
G10	2050 [45]
6934485	1970 [44]
6302341-1	2110 [46]
6302341-5	2150 [46]

Figure 29. Compton Scattered Radiation of Copper Trace on G10 Substrate

4.4.4 Test with Ring-Slit Camera and Scintillator Detector

4.4.4.1 Experimental arrangement

In this experiment, a slightly different design of the ring-slit camera shown in Figure 24, was constructed. This camera consists of the ring mask, CsI scintillator crystal, A2 PMT, and a power supply and amplifier; the Si array detector and the spring loaded displacement gages were not included. A collimator was made of a 2-mm Pb plate with a 0.5-mm hole in it that was placed 1.5 mm in front of the X-ray target of FeinFocus X-ray generator. The ring-slit camera was loaded on the five-axis manipulator of the X-ray generator. The two layered dummy circuit board was used in this experiment. The separation between the centers of the two copper layers was 1.7 mm. The dummy circuit board was 1.5 mm in front of the collimator. The zero reference position for the ring slit detector was the front surface of the dummy circuit board. The radius of the ring slit in the front was 4.7 mm. The slit has a 45 degree angle. Figures 30 and 31 show the layout dimensions and a photograph of the experimental arrangement. Figure 30 shows that the detector receives the maximum scattered signal from first layer of copper when it is 3 mm away from the zero position.
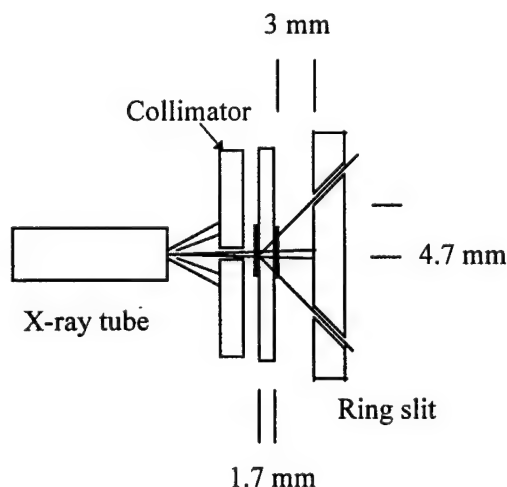

Figure 30. Experimental Arrangement

4.4.4.2 Depth resolution

The X-ray generator was set at 80 KeV and 0.1 mA. The ring-slit camera scanned through the depth of the dummy circuit board over a distance of 7.4 mm with a step size of 245 μm. Figure 31 shows a typical energy spectrum of the Compton scattered X-ray light. Compared with the spectrum taken with the CZT detector shown in Figure 32, the resolution is much lower but the photon count is much higher.

Figures 33 and 34 show the profiles of the scattered X-ray intensity of the circuit board and the background as a function of depth. Surprisingly, they have similar features, for example, the roll off at about 7.4 mm position where a more flat feature is expected for the background. Several possible sources could have caused these features. One most likely source is the scattered light from the collimator. This is schematically illustrated in Figure 35. Not all the X-ray light from the collimator was collimated, a small fraction of the X-ray light was reflected by the wall of the collimator and scattered into a solid angle, Ω. There is a high probability that the scattered X-ray would reach the scintillator through the ring

slit between position 1 and 2. As the ring slit is moved further away from the collimator, a steep drop of the reflected scattering is expected, due to both the inverse dependence of the intensity on the distance square and more importantly the fact that the angle of the reflection is much smaller than the angle of the slit. This scattering can be subtracted from the circuit board using the background signal.

Figure 36 shows the subtracted signal between Figure 34 (circuit board signal) and Figure 33 (the background signal). There are two peaks located at about 3 mm and 4.7 mm. The separation of the two peaks agrees with the separation of the two copper layers, and the position of the first peak (4.7 mm from the first copper layer) corresponds to the distance between the first copper layer and the front surface of the ring slit. This is the position where the scattering from the first layer ought to be detected (see Figure 30).

From the observation and analysis above, several conclusions can be drawn:

1. The photon counts increase significantly with the ring-slit camera and scintillation detector.
2. The depth structure can be resolved using Compton scattering.
3. Measures for noise reduction, such as shielding the scintillator in a thick Pb case, will improve the signal-to-noise level. Increasing the thickness of the ring-slit plate will also reduce the reflected noise.
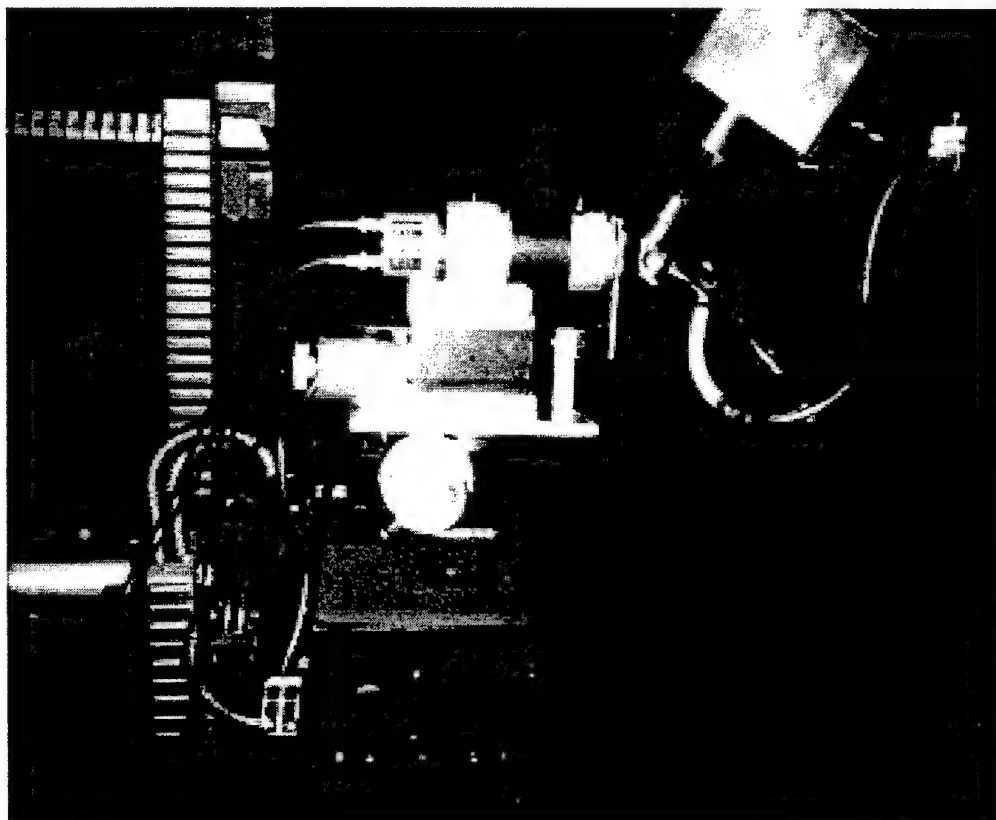

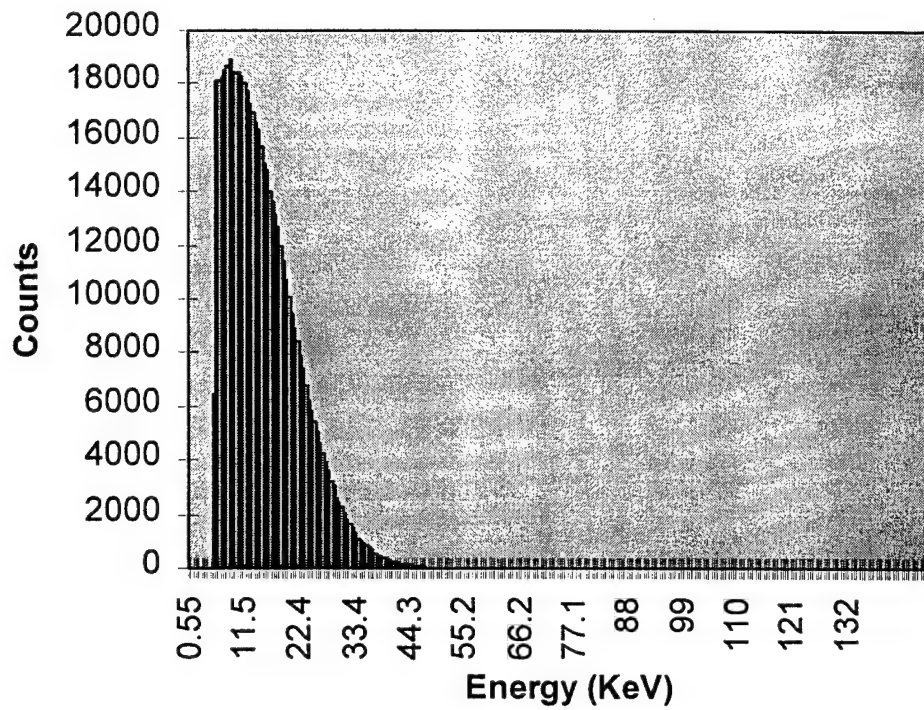**Figure 31. Experimental Setup for the Ring-Slit Camera**
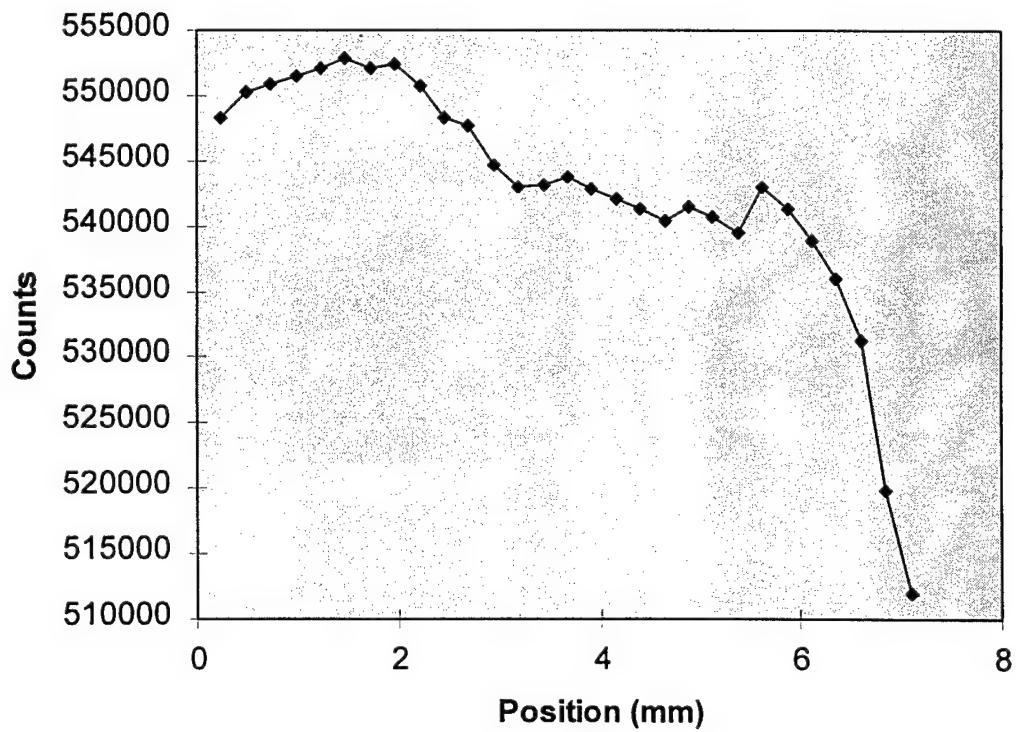
Figure 32. Spectrum of the Circuit Board

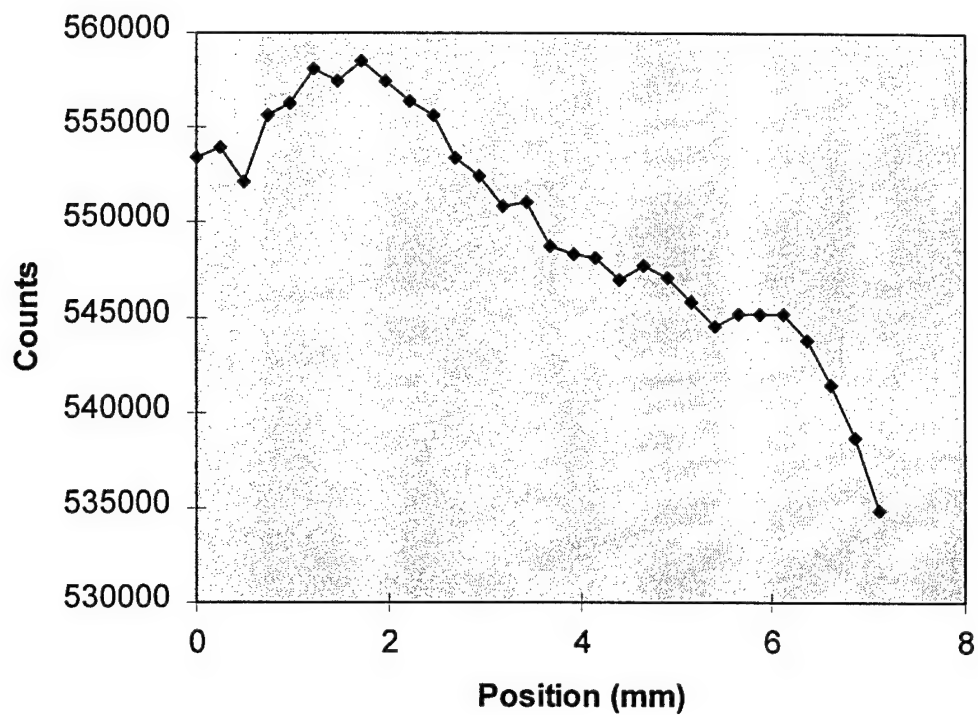**Figure 33. Background Signal**

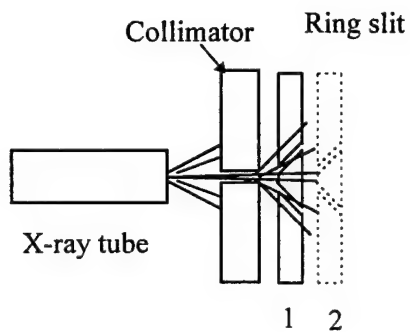**Figure 34. Signal of the Dummy Circuit Board**

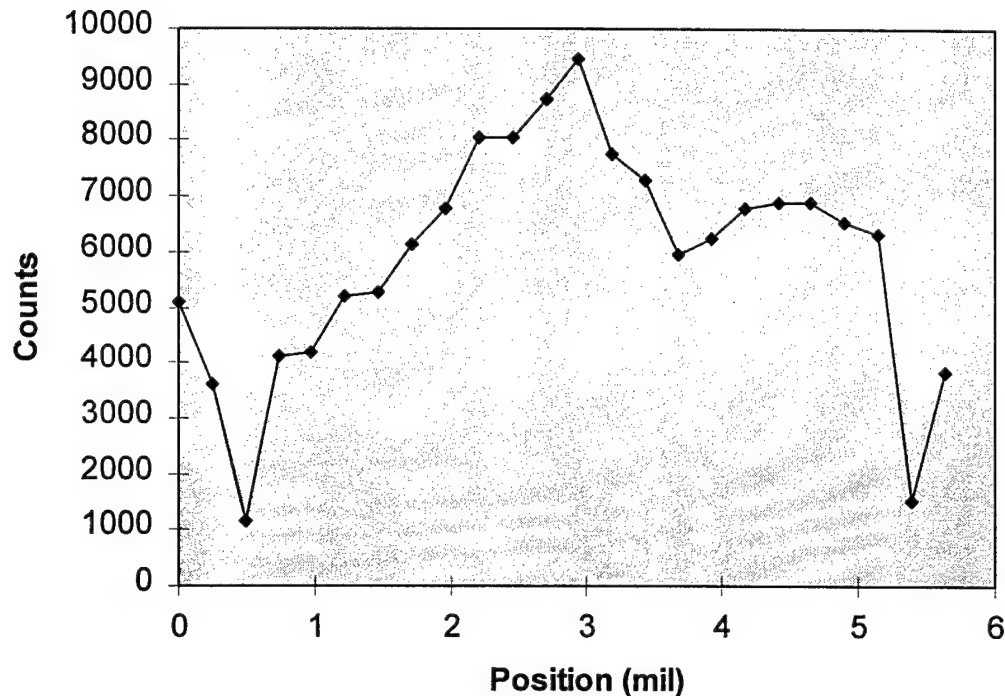**Figure 35. Scattered Light from the Collimator**

Figure 36. Subtracted Signal Between the Circuit Board Signal and the Background Signal

4.5 Task 5. Image Reconstruction

4.5.1 Image Reconstruction with Compton Scattering Data

The image reconstruction process is straightforward. The data acquisition process and image reconstruction process can be describe as follows.

First, the entire circuit board is divided into n by m by k voxels. The values n and m are determined by dividing the width of the finest trace into the sides of the circuit board. They should be twice the quotient. Signal processing theory demonstrates that no significant benefits will be gained by sampling at a frequency higher than the Nyquist frequency. The value k is taken as twice the number of layers for the same reason.

The detector position (particularly the depth) is calibrated through both mechanic and optical measurements. Then the layers of the circuit board are scanned in an orderly fashion (for example, row by row). The scattering intensity of each voxel along with its coordinate is recorded. This procedure is repeated for all the k layers.

The data so obtained will be evaluated layer by layer. For a voxel that contains either copper or G10, a binary value can be assigned to each voxel. Since the contrast between copper and G10 is expected to be more than a factor of two, such a threshold value can be found easily for each layer statistically. Note that the relative intensity for each layer is different due to the attenuation differences both before the layer and after.

However, for the voxels that contain a fraction of copper and a fraction of G10, ambiguity arises. In this case, the intensity of the voxel should be statistically different from either copper or G10. (The criteria need to be experimentally determined.) A new grid in the neighborhood of the voxel needs to be redrawn and more scans need to be taken until the ambiguity is eliminated.

This procedure will be repeated for all the data taken at different layers. A world view of the artwork can be thus reconstructed layer by layer for the entire circuit board.

The beauty of Compton scattering is simplicity. It requires minimum data processing. The entire image reconstruction process can be represented by the flow diagram in Figure 37.

However, in practice, the scanning speed of a Compton scattering image could be very time consuming (limited by X-ray sources). There are many ways to speed the image reconstruction processes. They include:

- Higher efficiency imaging system
- Higher intensity X-ray source
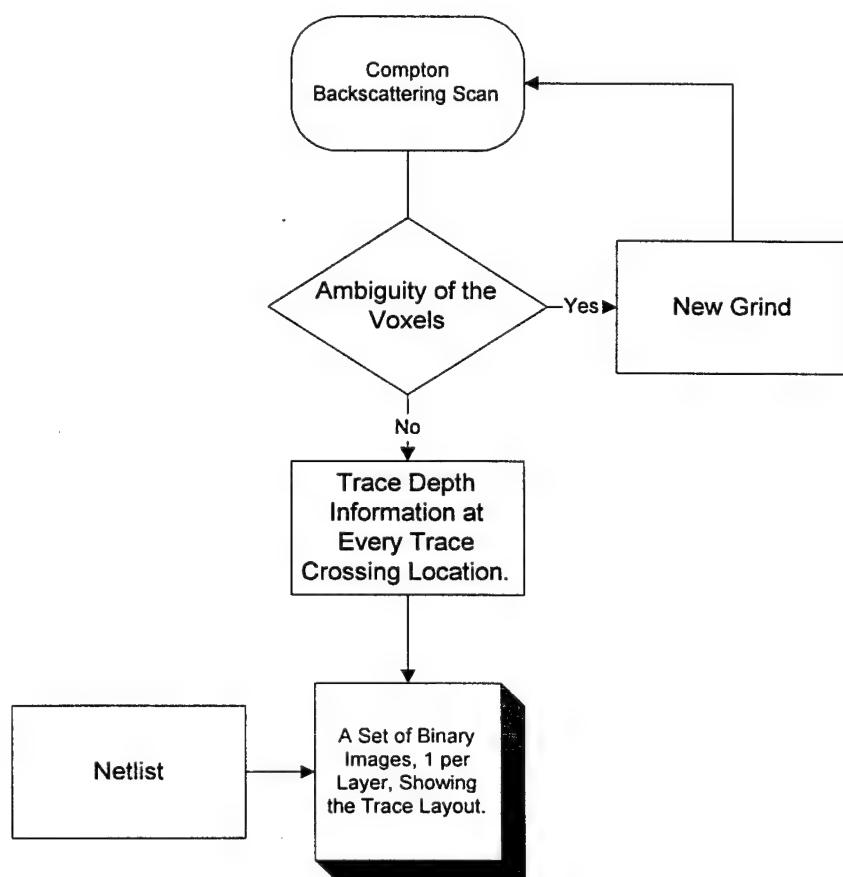- Combination of Compton scattering with other proven techniques

Figure 37. Flow Diagram for Image Reconstruction Using Compton Scattering

In the following, we will discuss using the technique of 2-D projection combined with Compton scattering. Figure 38 shows a 2-D projection of a circuit board. Only one point at each trace segment, such as AB in Figure 38, is needed for Compton scattering measurement to resolve its depth. The speed of image reconstruction using the combination of 2-D projection and Compton scattering will be many folds faster than using Compton scattering alone. This process is discussed in the next section.
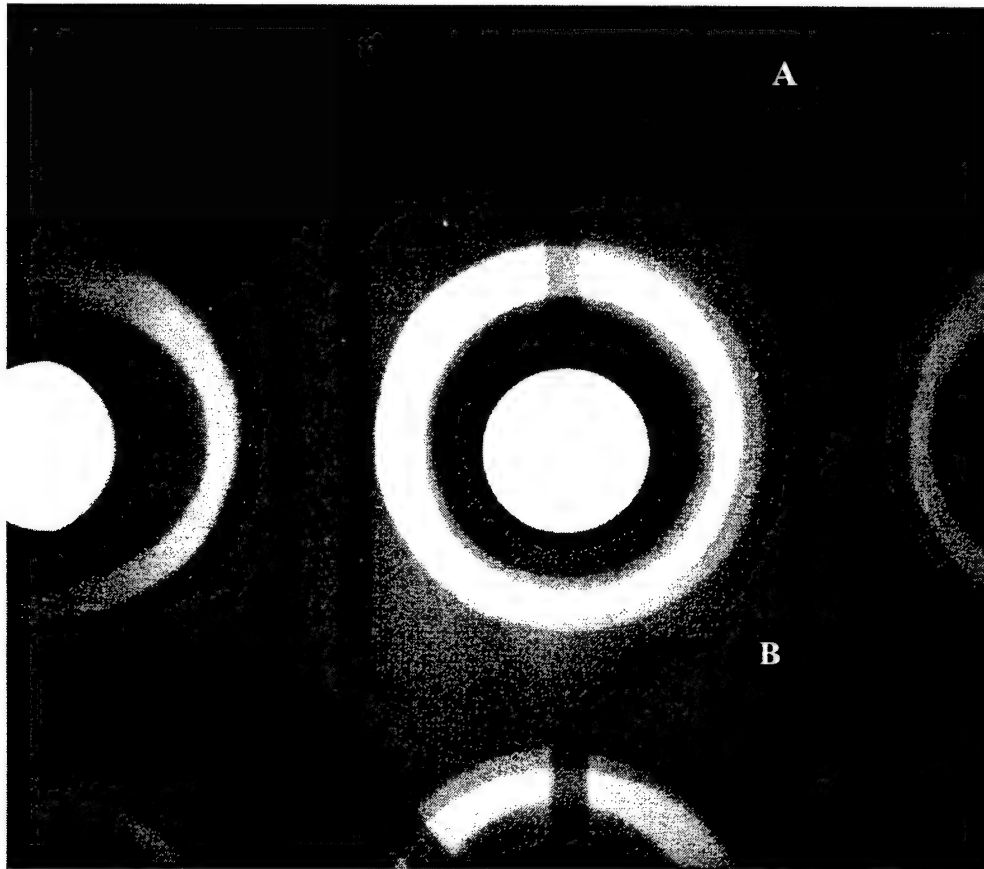

Figure 38. 2-D Projection of a Circuit

4.5.2 Image Reconstruction with a Combination of 2-D Projection Data and Compton Scattering Data

4.5.2.1 Create X-ray projection image

Scan X-ray head (using the Si array detector in the ring-slit camera) over circuit board and create a projection image, sampling at n by m grid as described in Section 4.5.1. This will create a 2-D orthogonal projection of the circuit board.

4.5.2.2 Image processing

The image processing routines will use the 2-D orthogonal projection image to produce a list of all through hole, via, 2-D projection trace locations, and trace crossing locations.

4.5.2.2.1 Detection of through hole and via locations

The detection of through hole and via locations from the 2-D projection image is a very simple image processing operation. The through hole and via locations appear in the projection image as solid circles of detector saturation. At each through hole and via location, the connecting traces will be marked as locations where Compton scattering will be used.

4.5.2.2.2 Detection of 2-D projection trace locations

The detection of trace locations in the projection image is a very well defined image processing problem. Traces in the projection image will have the following distinguishing characteristics:

- Constant width
- Composed of many segments of linear features
- Higher density material in trace than the circuit board
- Terminate only at via, through hole, surface mount pad, or connector

The presence or absence of a trace projection can also be provided by the characteristic peaks due to photoelectric effect. Furthermore, the number of the copper layers in the path of the X-ray can also be determined from the intensity of the transmitted X-ray, provided the incident beam is well calibrated.

4.5.2.2.3 Detection of trace crossing locations

The detection of trace crossing locations is a straightforward extension of the detection of the trace locations. It is defined as the coordinates where two or more traces meet.

4.5.2.3 Compton scattering inspection

Compton scattering will be used to determine the depth of each segment defined by two crossings (as AB in Figure 38). The intensity of the trace from 2-D projection can be used to determine how many layers are there for this projected trace. If it indicates there is only one layer. The vertical scan will be terminated once the depth is determined (instead of scanning through the whole depth of the circuit board).

Each through hole or via will require one Compton scattering inspection per trace that connects to the through hole or via.

4.5.2.4 Well posed search

Solving each layer's trace layout is now a well-posed search problem. For each interconnection in the netlist we have all the information needed to be able to draw that trace in the set of output images. Each output image will correspond to one of the layers in the circuit board.

Each interconnection in the netlist for the circuit board provides one trace routing problem for the search algorithm. An example case is given in Figure 39. The image in Figure 40 is obtained by taking the 2-D orthogonal projection image of the circuit board. Around each trace crossing in Figure 39, Compton scattering inspections at the seven sites shown will give the results listed in Table 7.

The whole process can be represented by the flow diagram in Figure 41. For additional speed, the circuit board can be subdivided into regions, and each region could be separately solved using parallel computing.
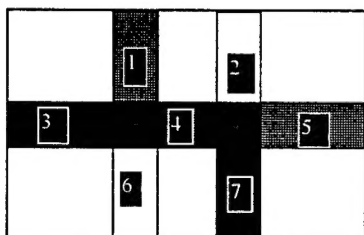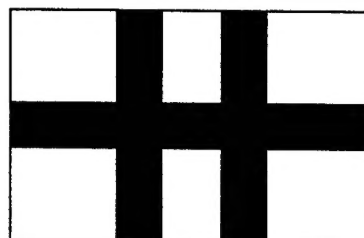

Figure 39. Actual Trace Layout

Figure 40. 2-D Projection Image

Table 7. Results from Compton Scattering Experiments

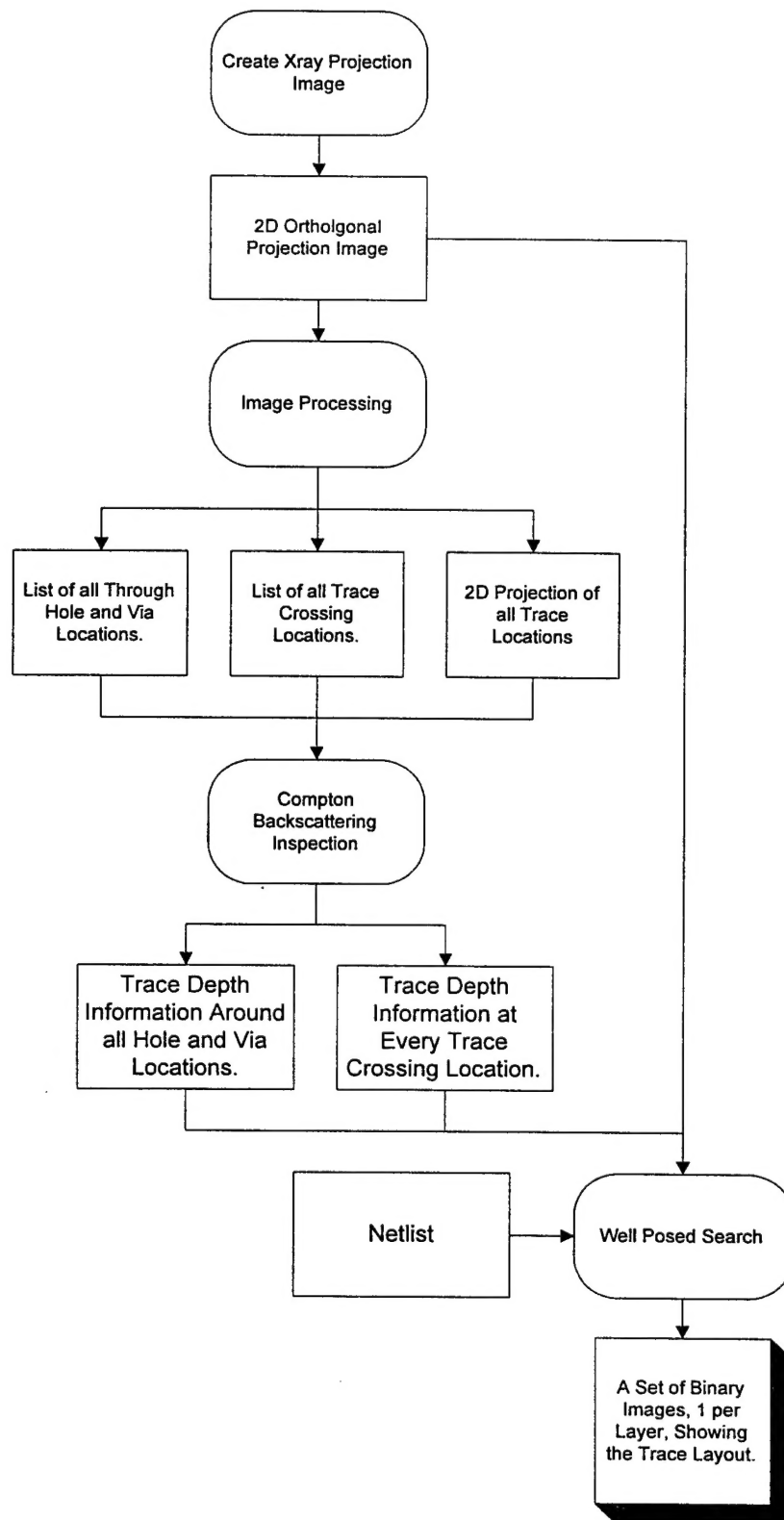| Position	Layer 1	Layer 2	Layer 3
1	no	yes	no
2	no	no	yes
3	yes	no	no
4	yes	yes	yes
5	no	yes	no
6	no	no	yes
7	yes	no	no

Figure 41. Flow Diagram for Image Reconstruction Using Combination of 2-D Projection and Compton Scattering

5. CONCLUSIONS

5.1 Technical Merits and Feasibility

During Phase I, we were able to satisfy all the technical objectives including the following:

1. We theoretically established the feasibility of imaging multi-layer printed circuit boards using Compton scattering. We also designed and constructed a high-efficiency, high-resolution ring-slit Compton scattering camera.

2. Experimentally verified the through-depth resolution of a layered structure of copper in a G10 substrate. With a high-intensity (e.g., full power of FeinFocus 160 KeV) and finely collimated X-ray beam, circuit boards with 122 microns spacing can be resolved.

3. An innovative, high-efficiency, unambiguous imaging algorithm was proposed to reconstruct the image of the layered structure. This algorithm can be easily structured to convert the layered images into Gerber files, which can be used by commercial machines to replicate the printed board.

5.2 Recommendations for Phase II Continuation

Based on our favorable Phase I results and the significant commercial opportunity to serve the government and the industrial community, we believe that it is appropriate to extend this program into Phase II, where a prototype high-efficiency, high-resolution Compton scattering camera will be built.